The effect of water vapor on methane adsorption in the nanopores of shale

Zhaodi Zhang[1] and Qingchun Yu[1]

[1]China University of Geosciences (Beijing)

November 24, 2022

Abstract

Key points: * The detrimental impact of preadsorbed water on the methane adsorption capacity and rate is more pronounced than that of water vapor * The distributions of adsorbed methane and water in shale pores were compared between the SAWM and PMMS * Water vapor preferentially enters mesopores (1.5-20 nm), and preadsorbed water mainly occupies micropores (0.3-1.5 nm) Abstract Water plays an essential role in shale gas migration and adsorption, and most studies on the influence of water on shale gas adsorption refer only to moisture-equilibrated shales. To investigate the impact of water vapor on methane adsorption in shales, three experiments were conducted and compared: (1) pure methane adsorption onto dry shale (PMD), (2) pure methane adsorption onto moisture-equilibrated shale (PMMS), and (3) simultaneous adsorption of water vapor and methane (SAWM) onto shale. Comparison of the experimental results reveals that the detrimental impact of water vapor on methane adsorption is inferior to that of preadsorbed water. Two mechanisms, i.e., water blocking and adsorption competition, are responsible for the reduction and difference in the methane adsorption capacity and adsorption rate between the PMMS and SAWM. Compared to the PMD, the methane adsorption capacity decreases by 81-96% in the PMMS, and by 20-49% in the SAWM. Methane adsorption equilibrium is achieved the fastest in the PMD. Before the equilibration degree reaches 95%, methane adsorption during the SAWM progresses more rapidly, while the reverse occurs when the equilibration degree exceeds 95%. The pore size distribution and water film thickness calculations indicate that the impacts of water vapor in the SAWM on micro-to mesopores are weaker than those of preadsorbed water. In the PMMS, adsorbed water mainly

The effect of water vapor on methane adsorption in the nanopores of shale

Zhaodi Zhang [1], Qingchun Yu [1]*

[1]Beijing Key Laboratory of Water Resources & Environmental Engineering, School of Water Resources and Environment, China University of Geosciences (Beijing), Beijing, 10083, China

*Corresponding author: E-mail: yuqch@cugb.edu.cn

Key points:

- The detrimental impact of preadsorbed water on the methane adsorption capacity and rate is more pronounced than that of water vapor
- The distributions of adsorbed methane and water in shale pores were compared between the SAWM and PMMS
- Water vapor preferentially enters mesopores (1.5–20 nm), and preadsorbed water mainly occupies micropores (0.3–1.5 nm)

Abstract

Water plays an essential role in shale gas migration and adsorption, and most studies on the influence of water on shale gas adsorption refer only to moisture-equilibrated shales. To investigate the impact of water vapor on methane adsorption in shales, three experiments were conducted and compared: (1) pure methane adsorption onto dry shale (PMD), (2) pure methane adsorption onto moisture-equilibrated shale (PMMS), and (3) simultaneous adsorption of water vapor and methane (SAWM) onto shale. Comparison of the experimental results reveals that the detrimental impact of water vapor on methane adsorption is inferior to that of preadsorbed water. Two mechanisms, i.e., water blocking and adsorption competition, are responsible for the reduction and difference in the methane adsorption capacity and adsorption rate between the PMMS and SAWM. Compared to the PMD, the methane adsorption capacity decreases by 81–96% in the PMMS, and by 20–49% in the SAWM. Methane adsorption equilibrium is achieved the fastest in the PMD. Before the equilibration degree reaches 95%, methane adsorption during the SAWM progresses more rapidly, while the reverse occurs when the equilibration degree exceeds 95%. The pore size distribution and water film thickness calculations indicate that the impacts of water vapor in the SAWM on micro- to mesopores are weaker than those of preadsorbed water. In the PMMS, adsorbed water mainly

occupies micropores (0.3–1.5 nm), and methane is adsorbed in pores larger than 1.5 nm. In the SAWM, methane preferentially occupies micropores; the competition between methane and water vapor is mainly concentrated in mesopores (1.5–20 nm).

Key words: simultaneous adsorption; moisture equilibration; water vapor; methane; adsorption rate

1 Introduction

Shale is a typical low-permeability crustal porous medium that strongly restricts mass transport and induces high pore pressures (Sun et al., 2020). Shales, as unconventional reservoir rocks, usually exhibit nanometer-scale pore sizes and a large specific surface area (SSA), and are characterized by a low permeability and high breakthrough pressure (Chalmers & Bustin, 2007). Shales are generally regarded as host rocks for high-level nuclear waste repositories and caprocks in carbon dioxide geological storage (Tsang et al., 2012). Due to the widespread occurrence of nanometer-scale pores, fluid transport in shale exhibits a significant difference from that in conventional rocks dominated by micrometer-scale pores (Zhang et al., 2020). Shale gas (mainly methane) occurs as free gas in pores and fractures, as adsorbed gas on the surface of organic matter and inorganic components and as a small amount of dissolved gas in water, oil, and bitumen (Dasani et al., 2017). Gas adsorption dynamics in shales play a key role in resource and environmental problems, and gas storage and transport differ notably in shale (Ma & Yu, 2020). The investigation of gas adsorption dynamics in shales is important to successfully accomplish methane recovery and carbon dioxide sequestration in shale gas reservoirs (Rani et al., 2018). Most experimental studies have suggested that the distribution and transport of water in shales play important role in the pore structure and chemical composition of shales, and water can further remarkably reduce the adsorption capacity and diffusivity of shale gas (Berghe et al., 2019; Liu et al., 2019). Therefore, the influence of moisture on methane adsorption in shales, and the mechanisms of gas-water-shale interaction should be investigated, which is beneficial to aquifer contamination control, geothermal energy production and carbon dioxide sequestration.

Water is an important component of gas shale reservoirs. The distribution of water can yield adverse impacts on the permeability and diffusivity of shale thereby reducing the gas adsorption capacity and prolonging the time required for gas to reach equilibrium. However, the issue of the effect of water in shales on the interaction between methane and shale surfaces remains unclear, but this phenomenon highly affects shale gas flow. Li et al. (2016a) analyzed the thermodynamic equilibrium between water films and water vapor in clay-rich shale pores and predicted the methane adsorption capacity at different water saturation levels in shale. The results indicated that methane adsorption onto clay-bound water films involves gas-liquid interaction. Gensterblum et al. (2014) presented a conceptual model to explain methane adsorption in the presence of water on coal. Their

results indicated that water tends to form hydrogen bonds with other adsorbed water molecules and surface-chemical matters. Only the surface chemistry (oxygen-containing functional groups) controls the competition between preadsorbed water and methane for adsorption sites. Wang et al. (2018) humidified three Carboniferous shale samples at five levels up to a relative humidity of 89% and tested their methane capacities under pressures up to 12 MPa. They suggested that water blocking in methane transport" and "surface competition in gas-solid interaction," are primarily responsible for methane capacity variations.

Many efforts have been focused on the adsorption and distribution of water in shale pores. For example, Sang et al. (2019) measured water vapor adsorption/desorption isotherms in five shales of the Illinois Basin. Their results suggested that water vapor adsorption in shale is controlled by the surface chemistry at low relative humidity levels through strong intermolecular bonding but is affected by pore structure at high relative humidity levels (> 0.9) through capillary condensation. Wang et al. (2020) analyzed the water distribution in coal, which indicated that water occurs as physically adsorbed water in micropores, water vapor retained in macropores and cleats, and capillary-bounded water confined in capillaries of the shale matrix. Li et al. (2016b) performed nitrogen sorption experiments to study the pore volumes occupied by water in shale. They concluded that a major difference in wettability occurs between inorganic and organic materials in shale, which directly results in a more complex water distribution in shale pores. The mechanisms by which various water distributions may impact the migration, adsorption and desorption of methane in shale have not yet been thoroughly investigated. Especially when water vapor and methane are simultaneously adsorbed in natural shale reservoirs, water vapor evaporates from liquid water and is adsorbed onto pore surfaces to displace methane (Kuchler, 2017; Vengosh et al., 2014). The diffusivity of methane and water vapor are affected, and the adsorption mechanism of methane and water vapor becomes more complicated. To date, most experimental studies on the detrimental influence of water on the shale adsorption capacity and dynamics have been based on the principle of immiscibility of water and methane, which have been conducted considering only moisture-equilibrated shales (i.e., preadsorbed water) (Gasparik et al., 2012; Tokunaga et al., 2017b; Yuan et al., 2014a). Data on the simultaneous adsorption process of methane and water vapor onto shale are scarce, and the understanding of the role of water on gas adsorption in shales remains insufficient. Hence, it is necessary to investigate the following two circumstances to better understand the water-

methane-shale interaction mechanism: (1) methane adsorption onto moisture-equilibrated shale and (2) simultaneous adsorption of water vapor and methane (SAWM) onto shale.

In this paper, experiments involving pure methane adsorption onto dry Shale (PMD), pure methane adsorption onto moisture-equilibrated Shale (PMMS) and SAWM were performed on three shale samples collected from the Qaidam Basin. Based on the experimental results, the effects of water vapor and preadsorbed water on methane adsorption were investigated. The methane adsorption capacity and adsorption rate in the PMD, PMMS and SAWM experiments were compared. Combining the calculation results of the pore size distribution and water film thickness, the distribution of adsorbed water and methane in shale pores during SAWM and PMMS were analyzed, and the mechanisms of water-methane-shale interaction during SAWM and PMMS were revealed. Water vapor and methane adsorption rates in the SAWM process were compared.

2 Methodology

2.1 Samples

The shale samples (S1, S2 and S3) in this study were collected in the Chaiye-2 core drilling well in the eastern Qaidam Basin, China. The samples were ground into 200 mesh and outgassed in an oven for 24 hours at 378.15 K prior to the initiation of the following experiments.

Geochemical tests were performed using several methods (Wang & Yu, 2020). The mineralogical composition and clay content were analyzed with a D8 DISCOVER X-ray diffraction analyzer based on the SY/T 5163-2010 standard. The total organic carbon (TOC) content was determined with a Leco SC-144DR carbon/sulfur analyzer based on the GB/T 19145-2003 standard. The maturity (characterized by the vitrinite reflectance) was quantified with a microphotometer (Hitachi F7000 MPV-SP) equipped with an oil-immersion objective lens based on the SY/T 5124-1995 standard. The kerogen types were determined with a biological microscope (Axioskop 2 plus) according to the SY/T 5125-1996 standard. Detailed information is provided in Table 1.

Table 1 Organic matter, mineralogical composition and clay content in the shale samples.

Samples	Depth (m)	TOC (%)	R_o (%)	Kerogen type	Total clay (%)	Q	Pl	Py	S	Clay content (%)			
										K	C	I	I/S
S1	911.07	1.23	1.34	II2	52	39	2	6	1	21	9	14	56
S2	957.80	0.38	1.27	II2	51	44	2	2	1	17	6	16	61
S3	1026.3	1.38	1.61	II2	37	32	1	2	28	24	11	17	48

R_o is the vitrinite reflectance, *Q* is quartz, *Pl* is plagioclase, *Py* is pyrite, *S* is siderite, *K* is kaolinite, *C* is chlorite, *I*

is illite, *I/S* is a mixed layer of illite and smectite.

According to the International Union of Pure and Applied Chemistry (IUPAC) (Sangwichien et al., 2002; Sing et al., 1985), nanopores in shales are divided into three grades: micropores (diameter ≤ 2 nm), mesopores (2 nm < diameter < 50 nm), and macropores (diameter ≥ 50 nm). Low-pressure carbon dioxide and nitrogen adsorption (LPA) and high-pressure mercury intrusion capillary pressure (MICP) tests were performed to calculate the pore size distribution. Although the MICP method can measure pores with diameters ranging from 3 nm to 200 μm, this approach does not accurately characterize ultra-small pores due to structural deformation under high pressures (Wang & Yu, 2016). CO_2 and N_2 molecules can access both micro- and mesopores in the low-pressure adsorption process (Yang & Yu, 2020). As a result, low-pressure CO_2 adsorption, low-pressure N_2 adsorption and high-pressure mercury intrusion techniques were applied to determine micro-, meso- and macropores, respectively. The SSA is largely attributed to micro- and mesopores (Gao & Yu, 2018), and CO_2 adsorption data were adopted to determine the SSA in this study. The intragranular porosity and skeletal density were determined via MICP tests (Schlömer & Krooss, 1997). LPA adsorption tests were conducted with an Autosorb-IQ-MP apparatus according to the GB/T 21650.2 and GB/T 21650.3 standards. MICP tests were conducted with an AUTO PORE IV 9520 mercury injection meter following the GB/T 21650.1-2008 standard. The isothermal LPA data were analyzed considering density functional theory (DFT) since this approach has been considered a more accurate method for pore size distribution analysis at the micro- and mesopore scales (Do & Do, 2003). The microstructure characteristics of the shale samples are given in Figure 1 and Table 2. The results indicate that the pore types in all the samples mainly include meso- and macropores. The portions of the micro- to mesopores account for 3.87-5.93% of the total pore volume.

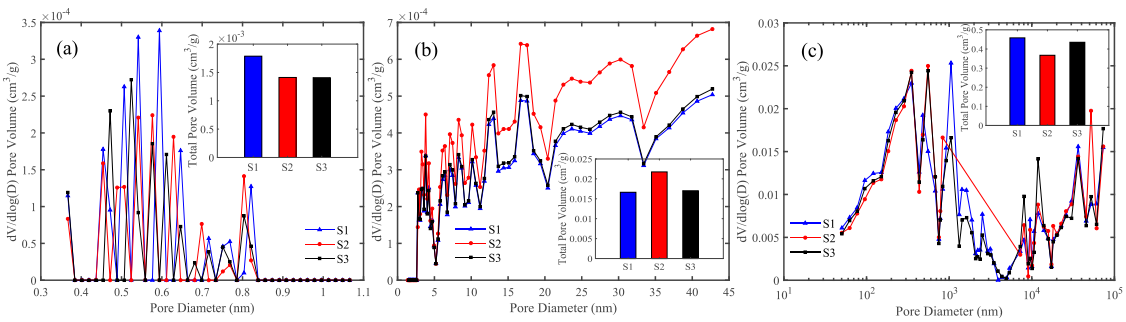

Figure 1. Pore size distribution and total pore volume of the shale samples. (a) Micropores, (b) mesopores, (c) macropores.

Table 2 Surface area, pore volume, intragranular porosity and skeletal density obtained via LPA and MICP.

Sample	Surface area (m^2/g)	Micropore volume (cm^3/g)	Mesopore volume (cm^3/g)	Macropore Volume (cm^3/g)	Intragranular porosity (%)	Skeletal density (g/mL)
S1	11.7647	0.0018	0.0166	0.4582	52.1918	2.1030
S2	10.1211	0.0014	0.0217	0.3673	42.8422	1.7737
S3	9.9033	0.0014	0.0170	0.4352	53.4421	2.3638

2.2 Experimental program

Adsorption experiments were conducted according to the GB/T 1560-2004 China national testing standard at the Beijing Key Laboratory of Water Resources and Environmental Engineering. A schematic of the apparatus is given in Figure 2. The experimental temperature is controlled at 313.15 K. The limits of the pressure and temperature are 10 MPa and 333.15 K, respectively. The adsorption system comprises receiver cell, adsorption cell, and high-precision pressure transducers with an accuracy of 0.001 MPa and an HC2A-IC102 relative humidity-temperature monitoring probe with accuracies of 0.01 K and 0.01 % (supplied by Rotronic, Switzerland). The inner volumes of the cells and pipelines were determined with the helium expansion method and amounted to 66.042 and 46.660 cm^3 for the receiver and adsorption cells, respectively.

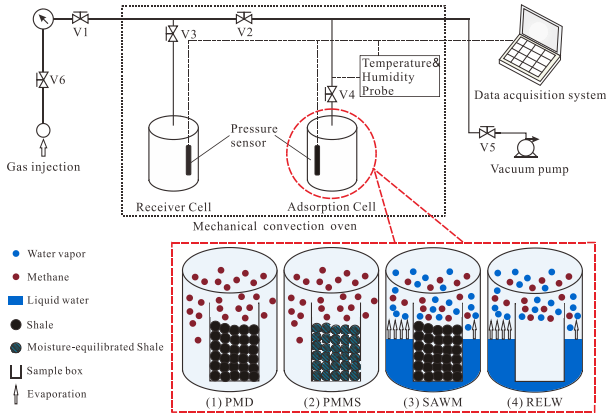

Figure 2. Schematic of the experimental apparatus.

Four experiments were designed in this study, namely, (1) PMD, (2) PMMS, (3) SAWM and (4) reference evaporation of liquid water (RELW) experiments. All of the above experiments were conducted at 1, 3 and 5 MPa.

The procedure of the PMD experiments can be found in Wang and Yu (2019).

In the PMMS experiments, moisture-equilibrated samples with four water saturation levels were prepared in a sealed desiccator at 313.15 K using saturated aqueous salt solutions of $MgCl_2$, NaBr, NaCl and K_2SO_4, and the relative humidity was controlled at 31.6%, 53.17%, 74.68% and 96.41%

(Greenspan, 1977). The water saturation in each shale sample was monitored via weighing. The moistening procedure was terminated when a constant sample mass was reached, after which the moisture-equilibrated sample was transferred to the sample cell. The remaining steps are the same as those for the PMD experiments. The water saturation of the samples (S_w) after the moistening procedure is listed in Table 3.

Table 3 Water saturation in the shale samples under the different relative humidities.

R_h	S_w (%)		
	S1	S2	S3
31.6%	2.09	1.62	1.15
53.17%	2.40	1.70	1.48
74.68%	2.68	1.92	1.58
96.41%	11.59	7.07	4.91

In the SAWM experiments, as shown in the enlarged details in Figure 3, the adopted CH_4-H_2O mixture produces a two-phase system in the adsorption cell: the upper part is a CH_4-H_2O gas mixture, and the lower part is liquid water. The procedure of the SAWM experiment is as follows:

(a) The adsorption system was vacuumed, pure methane was injected into the receiver cell through the regulating valve, and the stabilization time lasted 4 hours.

(b) Approximately 8 g of dried sample was placed in the sample box.

(c) The sample box and 6 mL of deionized water (the temperature of the deionized water was also 313.15 K) extracted with a calibrated pipette gun (calibrated with 299.15 K of deionized water) were placed in the adsorption cell.

(d) The sample box, temperature-relative humidity monitoring probe and adsorption cell were assembled. V2 was opened to allow the pure methane to flow into the adsorption cell. Pressure and temperature-relative humidity data points were recorded every 1 and 5 s, respectively. The data collection rate was subsequently increased to 10 s when the variations in pressure is not obvious.

(e) The experiment was terminated when the pressure decay rate fell below the resolution of the pressure sensor and the relative humidity increment rate within 24 hours was lower than 1%. The equilibrium moisture content in the sample was immediately weighed with an electronic balance.

(f) All the above experimental steps were repeated, and the experiment on each sample under equilibrium adsorption pressures of 1, 3 and 5 MPa was completed.

RELW experiments at 1, 3 and 5 MPa were correspondingly conducted to determine the

relationship between the evaporation rate of liquid water and the relative humidity in the adsorption cell. This relationship was considered when calculating the adsorption amount of water vapor in the SAWM experiments. The procedure of the RELW experiment is the same as that of the SAWM experiment except that there is no sample in the sample cell.

2.3 Analysis method of the experimental data

2.3.1 Relationship between the water vapor saturation pressure and methane partial pressure in the adsorption cell

In terms of the water vapor-methane gas mixture contained in the adsorption cell, the saturated water vapor pressure is affected by the partial pressure of methane, leading to variation in the relative humidity and evaporation rate of liquid water in the adsorption cell. Therefore, the relative humidity and saturated water vapor pressure in the adsorption cell should to be calibrated to obtain the evaporation rate of liquid water in the adsorption cell. The chemical potentials of liquid water and water vapor should be equal when phase equilibrium is reached. If the total pressure of the mixture increases by ΔP_m, when phase equilibrium is again reached, the chemical potentials between the two phases are given as:

$$u^l + (\frac{\partial \mu^l}{\partial P_m})_T dP_m = \mu^g + (\frac{\partial \mu^g}{\partial P_m})_T dP_m \tag{1a}$$

$$(\frac{\partial \mu^l}{\partial P_m})_T = (\frac{\partial \mu^g}{\partial P_m})_T = (\frac{\partial \mu^g}{\partial P_s})_T (\frac{\partial P_s}{\partial P_m})_T \tag{1b}$$

where u^l and μ^g are the chemical potentials of liquid water and water vapor respectively, and P_s is the saturated vapor pressure of water, which is expressed as (Shibue, 2003):

$$ln\left(\frac{P_s}{P_c}\right) = \frac{T_c}{T}(a_4\tau + a_5\tau^{1.5} + a_6\tau^3 + a_7\tau^{3.5} + a_8\tau^4 + a_9\tau^{7.5}) \tag{2}$$

where $\tau = 1 - T/T_c$, the critical pressure P_c and critical temperature T_c of water are equal to 22.064 MPa and 647.096 K, respectively, a_4=−7.859, a_5=1.844, a_6=−11.786, a_7=22.680, a_8=−15.961, and a_9=1.801.

The molar volume of liquid water can be regarded as a constant since the compressibility of liquid water is very low. According to the relationship between the molar volume and the chemical potential and equation of state, Eq. (2b) can be rewritten as:

$$\frac{RT}{P_s} dP_s = V_m^l dP_m \tag{3}$$

where V_m^l is the molar volume of liquid water (cm^3/mol).

If the methane partial pressure increases to P_m, the saturated vapor pressure of water changes from P_s to P_s', and the total pressure of the mixture changes from P_s to $P_s' + P_m$. Integration of the left and right sides of Eq. (3) from P_s to P_s' and P_s to $P_s' + P_m$, respectively, yields:

$$RTln\frac{P_s'}{P_s} = V_m^l(P_s' - P_s + P_m) \tag{4}$$

where P_s' is the new saturated vapor pressure of water after the methane pressure increases to P_m.

The partial pressure of water vapor P_w at the different methane pressure and temperature levels is calculated with:

$$P_w = P_s' R_h \tag{5}$$

where R_h is the relative humidity, which is measured in real time by the monitoring probe in the adsorption cell.

2.3.2 Adsorption amount of methane

Dalton's partial pressure law is adopted to calculate the partial pressure of CH_4 or H_2O in the CH_4-H_2O mixture (Zhou et al., 2000), which is given by:

$$P_i V = Z_i N_i RT \tag{6}$$

$$y_i = \frac{P_i Z}{P Z_i} \tag{7}$$

where P_i is the partial pressure of gas component *i* (MPa), V is the bulk gas volumes (cm^3), Z_i is the compressibility factor of gas component *i* (dimensionless), N_i is the amount of gas component *i* (mol), *R* is the universal gas constant (KJ/mol·K), *T* is the temperature (K), y_i is the mole fraction of gas component *i* in the CH_4-H_2O gas mixture, P is the total pressure of the gas mixture (MPa), Z is the corresponding compressibility factor, and Z and Z_i are calculated in REFPROP software, which was provided by the National Institute of Standards and Technology (Heller & Zoback, 2014).

After obtaining the partial pressure of methane via the aforementioned theory, the amount of adsorbed methane is described as:

$$m_a = m_t - m_f \tag{8}$$

where m_a is the adsorption amount of methane in shale (mol), m_t is the total amount of free methane entering the adsorption cell from the receiver cell (mol), and m_f is the amount of residual free methane within the void volume of the adsorption cell (mol).

The Peng-Robinson (P-R) equation was considered to calculate m_f in the adsorption cell

(Stryjek & Vera, 1986):

$$P = \frac{RT}{V_m - b} - \frac{a}{V_m^2 + 2V_m b - b^2} \tag{9}$$

where $a = (0.457235R^2T_c^2/P_c)\gamma$, $b = 0.077796RT_c/P_c$, $\gamma = (1 + k(1 - T_r^{0.5}))^2$, $k = k_0 + k_c(1 + T_r^{0.5})(0.7 - T_r)$, $k_0 = 0.378893 + 1.4897153\omega - 0.17131848\omega^2 + 0.0196554\omega^3$, and V_m is the molar volume of the residual free methane in the adsorption cell (cm^3/mol).

The critical properties of methane and water are presented in Table 4. Mixing rules are crucial to extend the P-R equation from pure gas to gas mixtures, and one-fluid mixing rules are given in Eqs. (10)-(12). The interaction parameter C_{ij} for methane and water vapor equals to 0.485 (Daridon et al., 1993; Dhima et al., 1998, 1999; Peng & Robinson, 1976; Søreide & Whitson, 1992; ZareNezhad & Eggeman, 2006).

Table 4 Pure-fluid critical properties applied in the improved P-R equation.

	T_c (K)	P_c (bar)	ω	k_c
CH_4	190.555	45.95	0.01045	0
H_2O	647.286	220.8975	0.34380	-0.06635

$$a = \sum_i \sum_j y_i y_j a_{ij} \tag{10}$$

$$b = \sum_i y_i b_i \tag{11}$$

$$a_{ij} = (1 - C_{ij})\sqrt{a_i a_j} \tag{12}$$

Therefore, m_f in the adsorption cell can be obtained as:

$$m_f = \frac{y_m(V_s - \frac{m}{\rho_s})}{V_m} \tag{13}$$

where m is the mass of the shale sample (g), which is listed in Table 5, V_s is the remaining volume of the adsorption cell after deducting the volume of liquid water and the sample box (40.6598 cm^3), and ρ_s is the skeletal density of the sample (g/mL).

Table 5 Mass of the samples (g).

Sample	SAWM			PMD		
	1MPa	3MPa	5MPa	1MPa	3MPa	5MPa
S1	8.1565	8.7840	7.8200	9.0296	9.2287	9.1269
S2	8.2920	8.9081	8.3382	8.9007	8.7049	9.1398

2.3.3 Adsorption amount of water vapor

According to the law of mass conservation, the water vapor conversion process in the SAWM and RELW experiments can be described as:

$$w_a = w_e - w_f \tag{14a}$$

$$w_{er} = w_{fr} \tag{14b}$$

where w_a is the amount of adsorbed water in shale (mol), w_e is the evaporation amount of liquid water in the SAWM experiment (mol), w_f is the amount of residual free water vapor within the void volume of the adsorption cell in the SAWM (mol), w_{er} is the evaporation amount of liquid water in the RELW experiment (mol), and w_{fr} is the amount of free water vapor in the RELW experiment (mol).

Eqs. (14a) and (14b) can be recast into integral form as:

$$\int_0^t v_a\, dt = \int_0^t v_e\, dt - \int_0^t v_f\, dt \tag{15a}$$

$$\int_0^t v_{er}\, dt = \int_0^t v_{fr}\, dt \tag{15b}$$

where v_a is the adsorption rate of water in shale (mol/s), v_e is the evaporation rate of liquid water in the SAWM experiment (mol/s), v_f is the water vapor rate increment in the SAWM experiment (mol/s), v_{er} is the evaporation rate of liquid water in the RELW experiment (mol/s), and v_{fr} is the water vapor rate increment in the RELW experiment (mol/s).

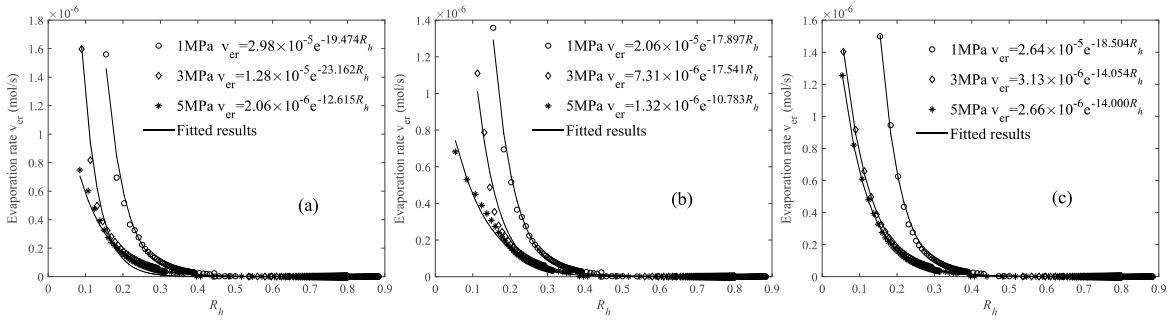

Figure 3. Relationship between the evaporation rate of water and R_h in the RELW experiment. (a) S1, (b) S2, (c) S3.

v_a cannot be calculated directly in the SAWM experiments since water vapor originating from liquid water is continuously absorbed onto the shale sample. As shown in Figure 3, the RELW experiment is designed to determine the relationship between the vapor-liquid conversion rate and R_h. The evaporation rate (the evaporation amount of liquid water per unit of time) is related to factors such as the temperature and relative humidity (Wang et al., 2015). According to Dalton's law of evaporation, the evaporation rate of liquid water is controlled by the relative humidity R_h. In the SAWM and RELW experiments, the evaporation conditions were identical except for the relative humidity. Hence, the evaporation rates in both experiments are the same when R_h in the SAWM experiments is the same as that in the RELW experiments:

$$v_e(R_h) = v_{er}(R_h) \tag{16}$$

The v_e value under the different pressures is obtained by substituting the experimentally obtained R_h data into the expressions shown in Figure 3. v_f and v_{fr} can also be obtained with the improved P-R equation. Finally, the amount of adsorbed water in shale can be obtained through Eq. (14a).

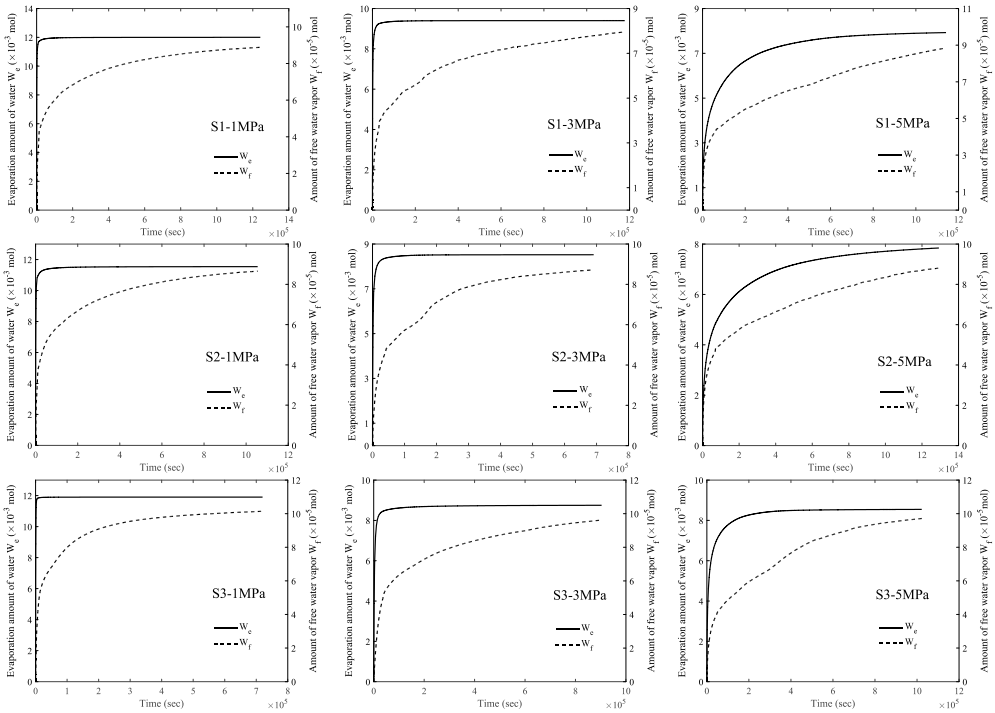

Figure 4. Amount of water evaporation (w_e) and free water vapor (w_f) in the adsorption cell in the SAWM experiments.

Figure 4 shows the calculation results for w_e and w_f in the SAWM experiments. The sample was removed from the adsorption cell and weighed immediately after equilibrium was reached to determine the equilibrium adsorption amount of water vapor of the shale sample (w_{ae}). The w_{ae} values that determined with the two methods are compared in Figure 5, which shows that the deviation is smaller than 5%.

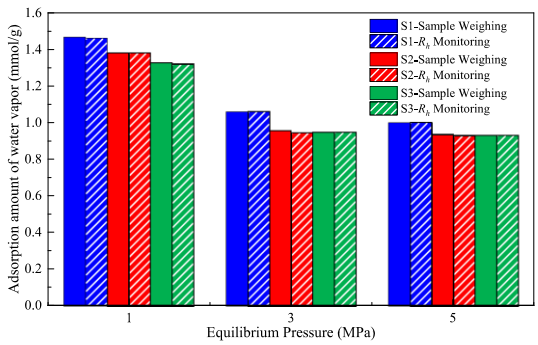

Figure 5. Comparison of the w_{ae} results obtained via sample weighing and R_h monitoring.

3 Experimental results and discussions

3.1 Experimental results

Figure 6 shows the experimental results for the methane adsorption capacity in the PMD experiments. Figure 7 depicts the experimental results for the methane and water vapor equilibrium adsorption amounts in the SAWM experiments. Figure 8 provides the experimental results for the methane equilibrium adsorption amount in the PMMS experiments. Figure 6 shows that S2 attains the highest methane adsorption capacity, followed by S1 and S3, and the methane adsorption capacity of the three samples increases with increasing pressure. In the SAWM experiments, as shown in Figure 7, the adsorption amount of water vapor is obviously larger than that of methane. The adsorption amount of water vapor decreases with increasing pressure, and S1 attains the highest water vapor adsorption capacity, followed by S2 and S3. In the PMMS experiments, as shown in Figure 8, the methane adsorption capacity decreases with increasing water saturation. Comparing Figures 6–8, it is found that methane adsorption amount in the PMD experiments is the largest, followed by the SAWM and PMMS experiments.

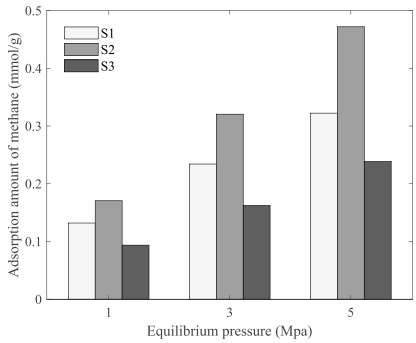

Figure 6. Equilibrium adsorption amount of methane in the PMD experiments.

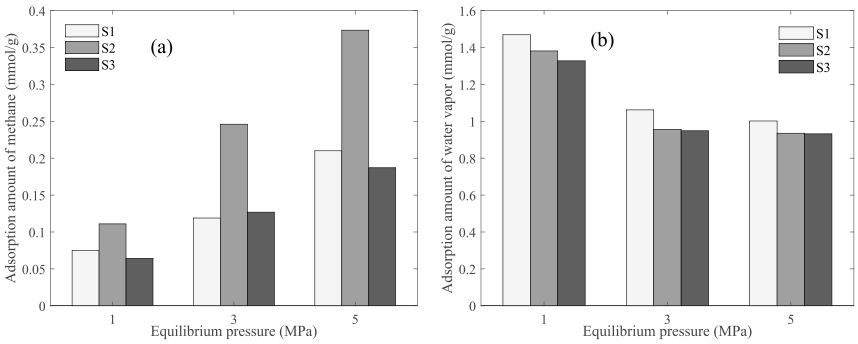

Figure 7. Equilibrium adsorption amount of methane and water vapor in the SAWM experiments. (a) Methane, (b) water vapor.

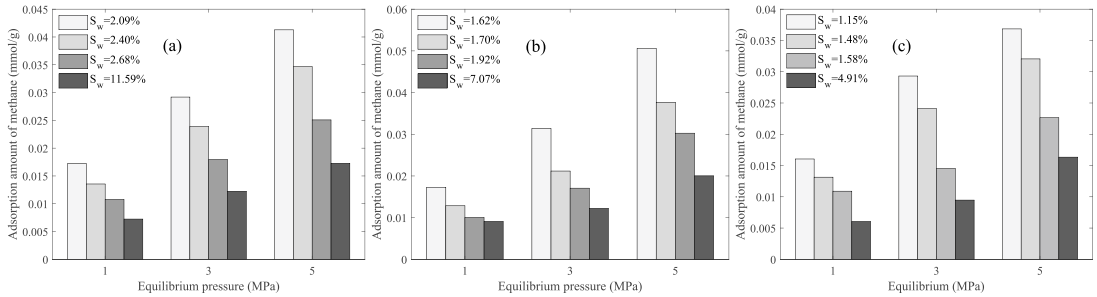

Figure 8. Equilibrium adsorption amount of methane in the PMMS experiments. (a) S1, (b) S2, (c) S3.

Figure 9 shows the variation in the methane and water vapor adsorption amounts over time in the SAWM experiments. Figures 10–11 show the variation in the methane adsorption amount over time in the PMD and PMMS experiments. The increase in the obtained methane adsorption curves is initially linear, after which the slope begins to decrease, eventually approaching zero. In the PMMS experiments, the lower the water saturation, the sooner the process attains equilibrium. In the SAWM experiments, the adsorption process of water vapor decelerates with increasing pressure.

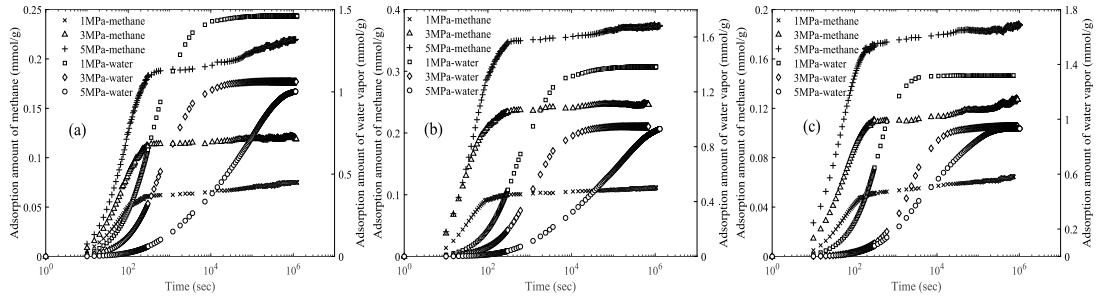

Figure 9. Adsorption amounts of methane and water vapor versus time in the SAWM experiments. (a) S1, (b) S2, (c) S3.

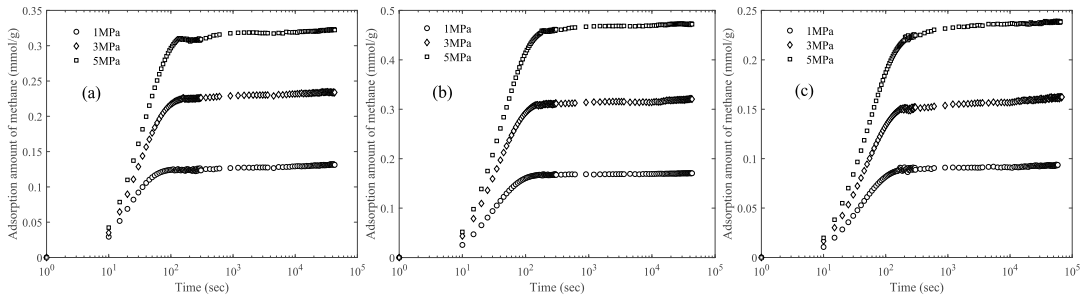

Figure 10. Adsorption amount of methane versus time in the PMD experiments. (a) S1, (b) S2, (c) S3.

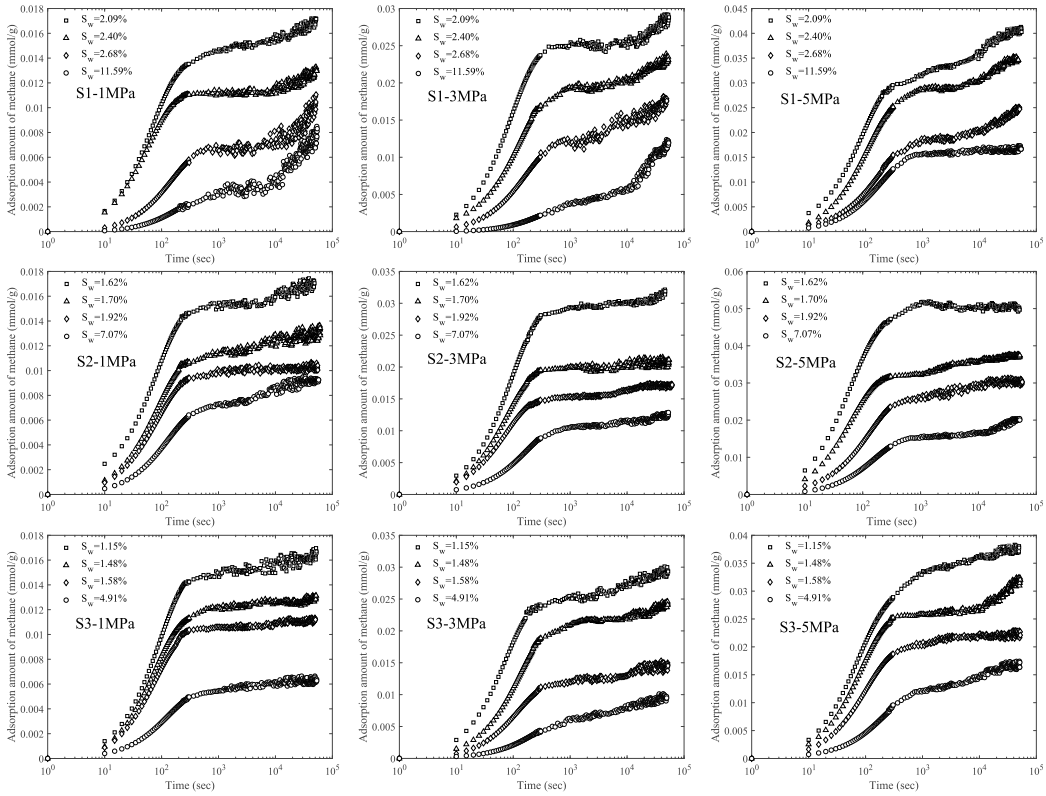

Figure 11. Adsorption amount of methane versus time in the PMMS experiments.

3.2 Methane adsorption capacity in the PMD, PMMS and SAWM experiments

Figure 12 shows the variation in the methane adsorption amount with the water content. The methane adsorption capacity of the moisturized samples is lower than that of the dry samples and decreases with increasing water content. In the PMMS experiments, the relation between the water content and methane adsorption amount approximately follows a power function with varying exponents (the PMD experiment can be considered a special case of the PMMS experiment at a water content of zero). In the PMMS experiments, the methane adsorption capacity decreases from 0.132–0.322 mmol/g under dry conditions to 0.007–0.017 mmol/g at the highest water level for S1, the methane adsorption capacity decreases from 0.171–0.472 mmol/g to 0.009–0.020 mmol/g for S2, and it decreases from 0.093–0.239 mmol/g to 0.006–0.016 mmol/g for S3. Initially, the methane adsorption capacity distinctly decreases with the water content. As the water content is continuously increased, the impact of preadsorbed water on the methane adsorption capacity gradually becomes less obvious.

As shown Figure 12, other studies related to the effect of preadsorbed water on the methane adsorption capacity of shales (Ma & Yu, 2020; Wang et al., 2018; Yang et al., 2017) were compared to our study. Ma and Yu (2020) investigated the adsorption dynamics of methane onto Carboniferous

shale under different water contents at 313 K and up to 9 MPa. Their results indicated that the decrease in the methane adsorption rate at low water saturations is larger than that at high water saturations. The diffusivity of methane decreases with the increase of water saturations, but the trend becomes weak at high water saturations. Yang et al. (2017) performed methane adsorption measurements on four Paleozoic shales with different water contents (dried and moisture equilibrated at relative humidities of 33%, 53%, 75%, and 97%) at 312 K and up to 25 MPa. They concluded that the variation in the methane adsorption capacity of shales with the water content can be divided into three stages: (1) initial decline stage, (2) steep decline stage and (3) slow decline stage. The slow decline stage of the four samples starts with a relative humidity of 75%, and the corresponding water contents in the samples are 0.88, 0.63, 0.71 and 1.01 mmol/g. These two studies indicate that additional preadsorbed water exerts little further influence on the methane adsorption capacity when the water content exceeds a certain critical value. The data given by Wang et al. (2018) exhibit a narrow distribution range, and their variation is not notable. They demonstrated that at R_h levels higher than 75% (the corresponding water content in the samples is 0.38, 0.18 and 0.54 mmol/g), moisture imposes a minimal influence on methane adsorption.

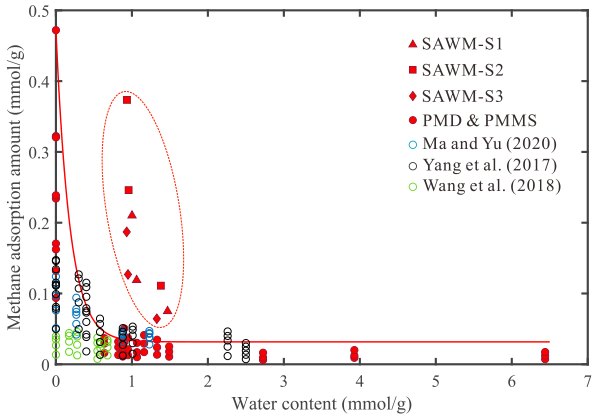

Figure 12. Relationships between the water content and methane adsorption amount determined by different authors (the data were cited from Ma and Yu (2020), Yang et al. (2017) and Wang et al. (2018)).

Authors have previously defined the critical water content, i.e., an additional amount of preadsorbed water does not further affect the methane adsorption capacity (Gasparik et al., 2012; Merkel et al., 2015, 2016; Ross & Marc Bustin, 2009). Beyond the critical water content, residual methane molecules become adsorbed at the sites occurring in hydrophobic kerogen, which is recognized as hydrophobic and exhibiting a preference for hydrocarbon gas. The majority of critical water content data ranges from 1.11 to 2.78 mmol/g (Feng et al., 2018). In our study, the effect of

preadsorbed water on the methane adsorption capacity becomes less obvious when R_h is higher than 74.68%, and the corresponding critical water contents for S1, S2 and S3 are 1.49, 1.07 and 0.88 mmol/g, respectively. Wang et al. (2018) suggested that the distribution of hydrophobic and hydrophilic sites throughout the pore network plays a key role in the effect of water on the methane adsorption capacity. The shale surface can be envisaged to contain water-prone and methane-prone sorption sites, with a partial overlap between these sorption sites (Wang & Yu, 2016). Water remarkably reduces the methane adsorption capacity by occupying these sites prior to the critical water content. When the water content continues to increase, the sites that can absorb both methane and water vapor increasingly become saturated, which do not further participate in water adsorption, thereby exerting a limited impact on the methane adsorption capacity.

It can be clearly seen that the variation trends in the PMMS and SAWM experiments are different. In the SAWM experiments, with increasing water content, the reduction in the equilibrium methane adsorption amount does not markedly decrease, as observed in the PMMS experiments. In the SAWM experiments, the methane adsorption capacity decreases from 0.132–0.322 mmol/g under dry conditions to 0.07–0.21 mmol/g at the highest water content level for S1, the methane adsorption capacity decreases from 0.171–0.472 mmol/g to 0.11-0.37 mmol/g for S2, and it decreases from 0.093–0.239 mmol/g to 0.06–0.19 mmol/g for S3. The methane adsorption amount is affected by both the pressure and water content in the SAWM experiments. The water content increases and the methane adsorption amount decreases with decreasing pressure, which leads to a more obvious reduction in the methane adsorption amount with the water content. The variation range of the water content in the SAWM experiments is narrower than that in the PMMS experiments, which is attributed to the inhibiting effect of methane on the evaporation of liquid water, i.e., the critical water content is not reached in the samples in the SAWM experiments. The methane adsorption amount in the SAWM experiments is obviously larger than that in the PMMS experiments at the same water content, suggesting that the negative impact of water vapor on the methane adsorption capacity of the shale samples is inferior to that of the preadsorbed water amount.

The equilibrium methane adsorption reduction during SAWM and PMMS compared to PMD were calculated with Eqs. (17) and (18), respectively, and the calculation results are listed in Table 6. The reduction ranges from 81–96% in the PMMS experiments, while it ranges from 20–49% in the SAWM experiments. It is generally accepted that, in addition to kerogen materials, inorganic

materials such as clay minerals could provide an additional adsorption amount in shale media due to the high internal specific surface area (Curtis et al., 2011; Ji et al., 2012). Either organic or inorganic materials could dominate the methane adsorption capacity under dry conditions, while the adsorption capacity of clay minerals decreases by 80–95% over dry conditions (Ross & Marc Bustin, 2009). Merkel et al. (2015) conducted methane sorption experiments at different water contents and observed the effect of moisture on the methane adsorption capacity of marine Bossier shale. The results indicated that moisture-equilibration at 97% R_h and 318 K results in a 78% loss of the methane adsorption capacity of the tested Bossier shale. They suggested that even very small water amounts can exert a major impact on methane adsorption capacity of shale. Gasparik et al. (2014) also reported that the methane adsorption amount in clay-rich shale notably decreases approximately 40%–90% under water-bearing conditions. The above results are consistent with our observations that water in clay-rich shale plays a key role in determining the methane adsorption amount.

$$R_s(\%) = \frac{m_{de} - m_{se}}{de} \times 100 \tag{17}$$

$$R_p(\%) = \frac{m_{de} - m_{pe}}{de} \times 100 \tag{18}$$

where R_s is the equilibrium methane adsorption reduction in the SAWM experiments, (%); R_p is the equilibrium methane adsorption reduction amount in the PMMS experiments, (%); m_{de} is the equilibrium methane adsorption amount in the PMD experiments, (mmol/g); m_{se} is the equilibrium methane adsorption amount in the SAWM experiments, (mmol/g); and m_{pe} is the equilibrium methane adsorption amount in the PMMS experiments, (mmol/g).

Table 6 Reduction in equilibrium methane adsorption in the SAWM and PMMS experiments compared to the PMD experiments.

Pressure	Sample	R_s	R_p			
			R_h=31.60%	R_h=53.17%	R_h=74.68%	R_h=96.41%
1MPa	S1	43.175	86.960	89.730	91.837	94.510
	S2	34.917	89.864	92.466	94.110	94.662
	S3	30.821	82.865	85.975	88.364	93.545
3MPa	S1	49.214	87.535	89.792	92.335	94.769
	S2	23.239	90.215	93.394	94.675	96.184
	S3	21.838	81.945	85.157	91.051	94.167
5MPa	S1	34.837	87.193	89.245	92.218	94.638
	S2	20.868	89.283	92.019	93.590	95.756
	S3	21.637	84.562	86.572	90.513	93.154

In the premoistening process, adsorbed water is prioritized over methane in the occupation process of adsorption sites, which reduces the methane adsorption capacity and methane-surface interaction. Even at an R_h level of 31.6%, the reduction in the methane adsorption amount in the PMMS experiments is also notable. Gensterblum et al. (2014) performed methane adsorption experiments on coal samples under dry and moisture-equilibrated conditions, and the interaction between preadsorbed water and methane on the coal surface involved volumetric displacement independent of the gas type. In the SAWM experiments in our study, although water vapor lowers the adsorption force between methane and shale surfaces, high methane pressures destabilize the adsorbed water films on the shale surfaces and reduce the water film coverage. The low partial pressure of water vapor leads to insufficient diffusion and the incomplete occupation of methane adsorption sites. Water molecules in the SAWM experiments cannot block pathways or occupy adsorption sites in advance, as was observed in the PMMS experiments. As a result, the effective surface area of shale and the gas storage potential in the SAWM experiments do not decrease as notably as those in the PMMS experiments.

As shown in Figure 13, the I/S and quartz contents are positively correlated with the equilibrium methane adsorption reduction amount in the PMMS experiments. On the one hand, the illite/smectite mixed layer plays a favorable role in water vapor adsorption by retaining adsorbed water in interlayer pores (Wang et al., 2018), blocking microchannels and deteriorating clay surfaces. On the other hand, quartz exhibits a higher hydrophobicity than does the illite/smectite mixed layer, leading to water preferentially occurring as droplets that block pore throats (Wang et al., 2020). In the PMMS experiments, as a result, the increasing I/S and quartz contents prominently enhance the negative effect of pre-adsorbed water on the methane adsorption capacity. This correlation in the SAWM experiments is obviously weaker than that in the PMMS experiments, which suggests that the impact of water vapor on the methane adsorption capacity is less affected by the increase in the I/S and quartz contents. This occurs because in the SAWM experiments, the methane adsorption capacity is largely constrained by the competition between water vapor and methane molecules on the shale surface, resulting in a weaker interaction between water vapor and shale.

Figure 13 also shows that the micro- and mesopore volumes achieve a good correlation with the equilibrium methane adsorption reduction amount in the PMMS experiments, but this correlation is not obvious in the SAWM experiments. The micro- and mesopore volumes are positively correlated

with the equilibrium methane adsorption reduction amount in the PMMS experiments. However, the opposite trend is observed in the SAWM experiments. The analysis suggests that preadsorbed water and water vapor play different roles in the effect of moisture on the methane adsorption capacity in regard to pore channel blocking. In the PMMS experiments, the increasing micro- and mesopore volumes enhances the impact of preadsorbed water on the methane adsorption capacity, indicating that preadsorbed water reduces the methane adsorption capacity via pore filling. In the SAWM experiments, the increasing micro- and mesopore volumes lowers the negative effect of water vapor on the methane adsorption capacity, but the effect of the micro- and mesopore volumes is limited. This occurs because the increase in micro- and mesopore volumes provides more sorption sites for methane-water vapor competition, which could simultaneously accommodate more adsorbed methane and water.

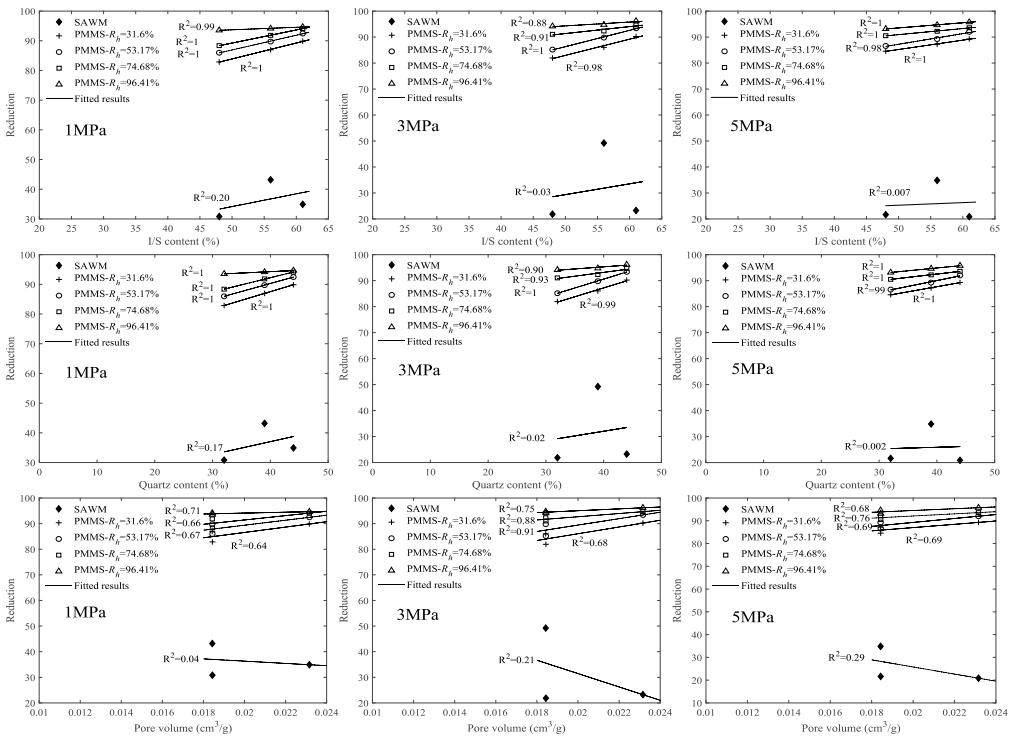

Figure 13. Correlation of the I/S and quartz contents and the pore volume below 40 nm (using both carbon dioxide adsorption and nitrogen adsorption data) with decreasing equilibrium methane adsorption.

3.3 Methane adsorption rate in the PMD, PMMS and SAWM experiments

Variations in the methane adsorption rate over time and with the water content are shown in Figure 14. The methane adsorption rate at the initial time increases with increasing pressure and decreases with increasing water content. In addition, the methane adsorption rate decreases with increasing time and water content. In the SAWM experiments, the decay in the methane adsorption

rate over time is alleviated with increasing pressure. In terms of the relationship between the water content and methane adsorption rate in the SAWM experiments, high pressure results in the methane adsorption rate decaying more rapidly with the water content. The methane adsorption rate at the initial time in the PMD experiments is the highest, followed by the SAWM and PMMS experiments. During the first 1000 s, the decline in the methane adsorption rate over time in the PMD experiments occurs the fastest, followed by the SAWM and PMMS experiments, indicating that the methane flow rate is obviously reduced by moisture, thereby prolonging the time required for methane to reach adsorption equilibrium. The comparison of the SAWM and PMMS experiments reveals that the methane flow rate and nanopore channels are less susceptible to water vapor at the early stage of the adsorption process.

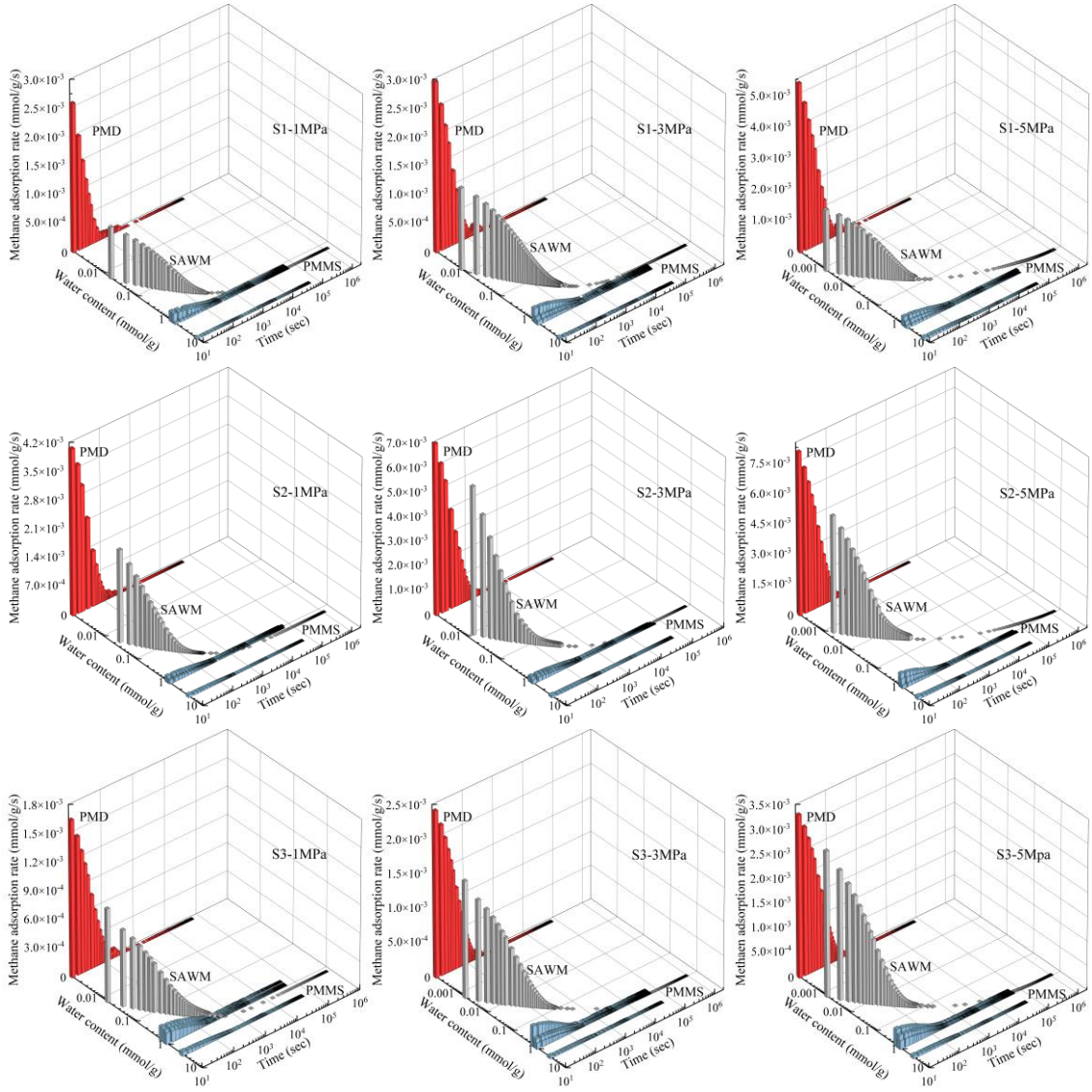

Figure 14. Variation in the methane adsorption rate with time and water content in the PMD, PMMS and SAWM experiments.

The ratio of the methane adsorption amount (m_x) to the equilibrium methane adsorption amount (m_{ae}) is referred to as the equilibration degree (E_x) of the methane adsorption process. t_x denotes the time when x % of the equilibrium methane adsorption amount is achieved. In this study, x=10, 50, 80 and 95 was selected to investigate the methane adsorption rate in the PMD, PMMS and SAWM experiments, and the corresponding t_x values are shown in Figure 15. t_x is the smallest in the PMD experiments, suggesting that methane reaches adsorption equilibrium the fastest when methane is adsorbed onto dry shale. t_x increases with increasing relative humidity in the PMMS experiments. The t_x value in the SAWM experiments is smaller than that in the PMMS experiments until the equilibration degree reaches 95%, indicating that methane in the SAWM experiments can reach the adsorption sites more rapidly before E_{95} and that the weakening impact of preadsorbed water on methane adsorption rate is more prominent. The t_x value in the SAWM experiments is larger than that in the PMMS experiments when the equilibration degree exceeds 95%, suggesting that the weakening influence of water vapor on the methane adsorption rate in the SAWM experiments becomes prominent near the adsorption equilibrium. This phenomenon is explained as follows: owing to the continuous evaporation of water vapor, there remain certain adsorption sites for both water vapor and methane near the methane adsorption equilibrium. As a result, water vapor can replace some of the adsorbed methane molecules through the volume displacement effect, resulting in some adsorbed methane molecules being desorbed, and the time required for methane to reach adsorption equilibrium is prolonged. E_{80} and E_{95} are two important points in the methane adsorption process. Before E_{80}, free methane controlled by the concentration difference flows in the pore channels at a higher rate, and a large amount of methane is adsorbed onto any vacant adsorption sites. When E_{95} is reached, the available sites for further methane adsorption almost disappear, and the variation in adsorption amount and adsorption rate are the lowest. Here, v_{80} and v_{95} are proposed as follows:

$$v_{80} = \frac{m_{80} - m_{10}}{t_{80} - t_{10}} \tag{19}$$

$$v_{95} = \frac{m_{95} - m_{80}}{t_{95} - t_{80}} \tag{20}$$

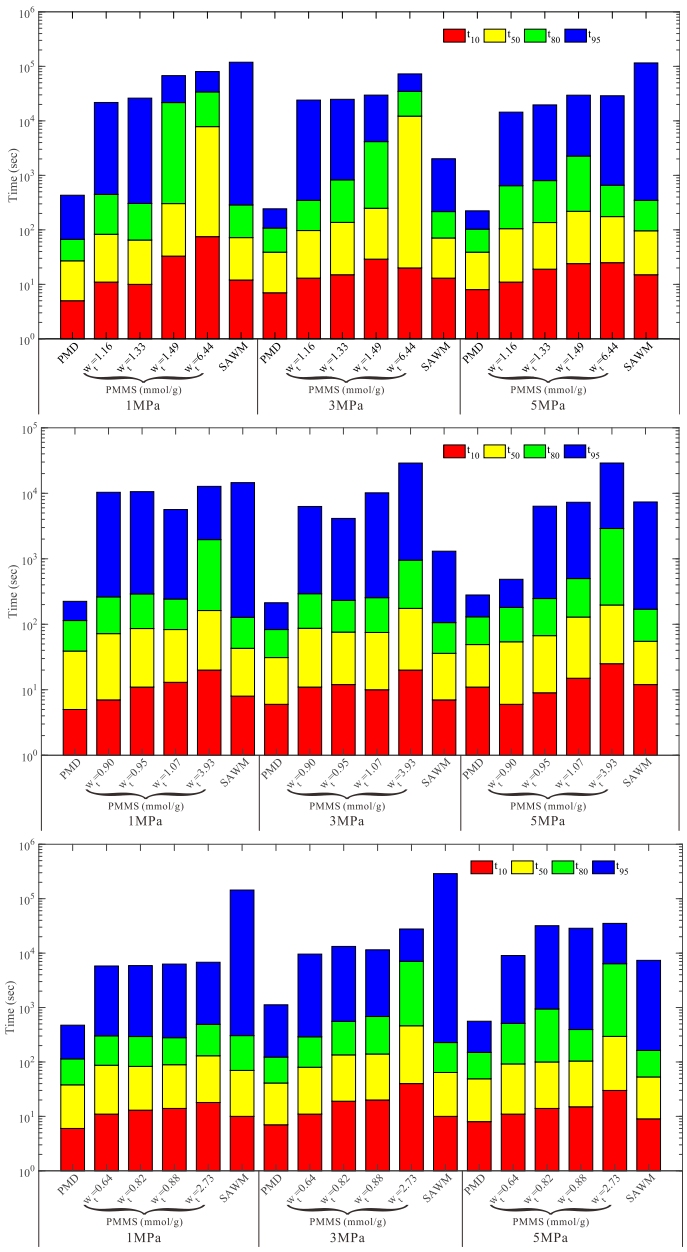

Figure 15. Values of t_{10}, t_{50}, t_{80} and t_{95} for methane in the PMD, PMMS and SAWM experiments. (a) S1, (b) S2, (c) S3.

As shown in Figure 16, v_{80} and v_{95} are negatively correlated with the TOC content, indicating that an increase in the TOC content reduces the methane adsorption rate, thus prolonging the time required for methane to reach adsorption equilibrium. Zou et al. (2018) concluded that organic matter contributes to the methane adsorption rate under high pressures within the initial time range. Our data indicate that the correlation of v_{80} with the TOC content is stronger than that of v_{95} with TOC the content, suggesting that the negative impact of the TOC content on the methane adsorption rate is more obvious at the early stage. Organic matter usually provides the initial dominant effective sites for methane (Wang et al., 2018). When E_{80} is achieved, these effective

sites tend to become saturated, and the micropores become increasingly blocked by the adsorbed methane and/or water, which results in an obvious restriction in methane transport. It can be inferred that an increase in the TOC content makes methane transport more susceptible to the accumulated gases. When E_{95} is achieved, the potential energy difference between the adsorption sites is relatively small, and the adsorption rate is mainly controlled by the interface interaction rate (Ma & Yu, 2020), resulting in the negative impact of the TOC content on methane transport near the adsorption equilibrium becoming insignificant.

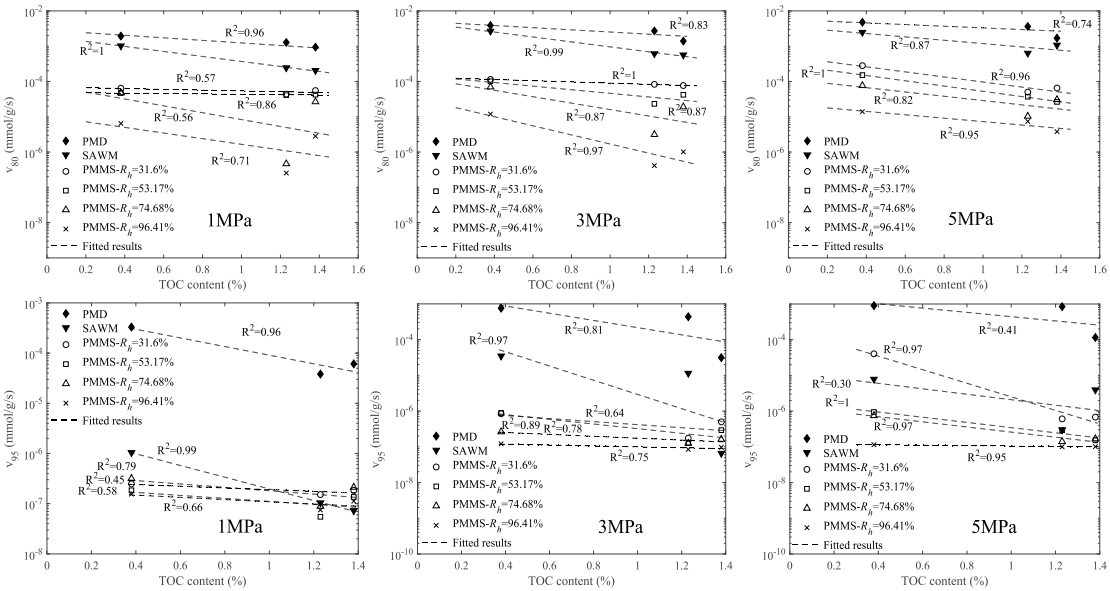

Figure 16. Correlation of the TOC content with v_{80} and v_{95}.

As shown in Figure 17, the variation in the methane adsorption rate with the equilibration degree at varying water contents in the PMMS experiments is investigated. The methane adsorption rate in the PMMS experiments can be divided into two parts (linear and fluctuating parts). In the first part, due to the high potential energy of the adsorption sites and the high methane concentration gradient, the methane adsorption rate distinctly decreases as a liner function of the equilibration degree. A large portion of vacant sorption sites and a high methane flow rate increase the adsorption amount during this process. In the second part, bulk methane diffusion disappears, and surface migration becomes dominant. The vacant adsorption sites for methane are reduced, and the driving force is lower than that observed in the first part. With increasing water content, the time required for the first part decreases and the time required for the second part increases. Yuan et al. (2014b) applied the bidisperse diffusion model to simulate gas transport in shale samples. Their results suggested that the reduction in gas diffusion coefficient is attributed to water in the pore spaces reducing the

void spaces available for gas transport. This also possibly occurs because moisture can swell clay minerals, resulting in a reduced pore volume and pore throats. As a result, a notable increase in preadsorbed water reduces the diffusivity of methane and the proportion of vacant adsorption sites, resulting in a small diffusion distance of methane and weak interaction between methane molecules and the shale surface.

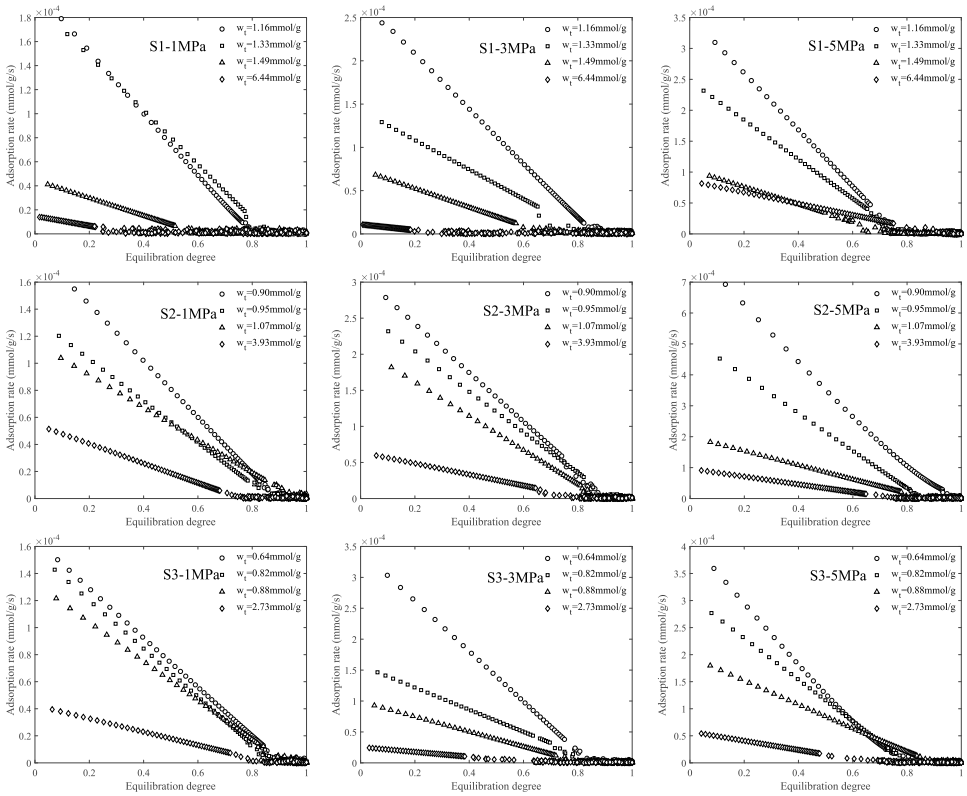

Figure 17. Variation in the methane adsorption rate with the equilibration degree in the PMMS experiments.

The variation in the methane and water vapor adsorption rates with the equilibration degree in the SAWM experiments was investigated, as shown in Figure 18. The variation in the methane and water vapor adsorption rates is closely related to the gas pressure. For S1 and S3, the water vapor adsorption rate is obviously higher than that of methane under 1 MPa, while the methane adsorption rate is higher than that of water vapor under 3 and 5 MPa. For S2, the methane adsorption rate is higher than that of water vapor under all pressure steps. The variations in the methane and water vapor adsorption rates in the SAWM experiments are different. Notably, the methane adsorption rate decreases linearly with the equilibration degree followed by a small-range fluctuation, and the water vapor adsorption rate decreases exponentially with the equilibration degree. Because the partial pressure of methane is much higher than that of water vapor, the inhibitory effect of methane on liquid water evaporation is obvious, and the driving force of water vapor toward bulk diffusion

is weak. Additionally, methane is usually attracted to shale surfaces via van der Waals forces. The cooperative nature of water enables water molecules to bond with oxygen-containing functional groups at adsorption sites with hydrogen bonds, in which hydrogen bonds are 5–10 times stronger than van der Waals forces (Švábová et al., 2011). The charged regions of clay minerals also absorb water molecules through the occurrence of interlayer spaces in clay minerals (Singh, 2016). Therefore, the difference in partial pressure, in addition to the difference in methane-shale and water-shale interaction mechanisms, are the main factors influencing the variation in the methane and water vapor adsorption rates in the SAWM experiments.

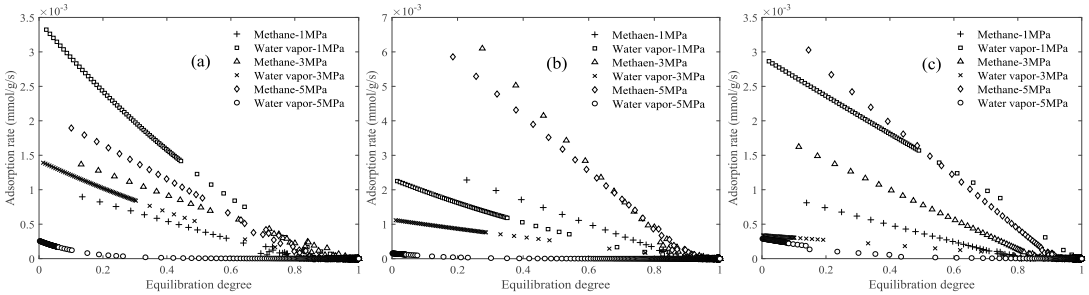

Figure 18. Variation in the methane and water vapor adsorption rates with the equilibration degree in the SAWM experiments. (a) S1, (b) S2, (c) S3.

Comparing Figures 17 and 18, it can be found that the variation in the methane adsorption rate with the equilibration degree in the SAWM experiments can also be divided into two parts (linear and fluctuating parts). However, the duration of the linear part in the PMMS experiments is shorter than that in the SAWM experiments. The comparison results suggest that the detrimental impact of preadsorbed water on the methane adsorption rate is more obvious than that of water vapor. This occurs because in the PMMS experiments, the increasing water film thickness during the premoistening procedure triggers water blocking, narrowing or even blocking of methane diffusion pathways, and seriously reduces the methane concentration gradient and methane-shale surface interaction. In the SAWM experiments, the diffusion and adsorption of water vapor in the pores is constrained by the high partial pressure of methane, and methane can reach the available adsorption sites more rapidly, thus reducing the detrimental effect of water on the methane adsorption rate. It is concluded that in the PMMS experiments, the impact of preadsorbed water on the methane adsorption rate is mostly reflected by the observed resistance and blocking effects. In the SAWM experiments, the impact of water vapor on the methane adsorption rate is largely reflected by the above inhibition and competition effects.

3.4 Distribution of adsorbed water in the shale pores in the PMMS and SAWM experiments

The distribution of adsorbed water and the interaction between liquid, gaseous and solid phases in shale pores have significant impacts in methane adsorption mechanisms. The distribution of adsorbed water in shale pores can be determined by combining the calculated water film thickness and pore size distribution. Based on the disjoining pressure theory, the relationship between the thickness of a water film and the relative humidity inside slit-shaped pores can be described as (Churaev et al., 2000; Tuller et al., 1999):

$$\prod_{slit}(h)\, V_m^l = -RTln(\frac{P_w}{P_s}) \tag{21}$$

where h is the water film thickness (nm), $\prod_{slit}(h)$ is the disjoining pressure between liquid film and solid surface within slit-shaped pores, which is related to h (MPa), and $\frac{P_w}{P_s}$ is the relative humidity of gaseous methane.

The disjoining pressure between the water film and shale solid surface comprises three parts (Derjaguin et al., 1987; Li et al., 2016b):

$$\prod_{slit}(h) = \prod_1(h) + \prod_2(h) + \prod_3(h) \tag{22}$$

where $\prod_{slit}(h)$ is the total disjoining pressure in slit-shaped pores, $\prod_1(h)$ denotes the van der Waals force, $\prod_2(h)$ is the electrical force, and $\prod_3(h)$ denotes the structural force.

The van der Waals force is approximately described by (Starov et al., 2007):

$$\prod_1(h) = \frac{A_H}{h^3} \tag{23}$$

where, A_H is the Hamaker constant in a gas/water/shale system (J).

In the circumstance of oppositely charged surfaces occurring at relatively small distances, the electrical force can be approximated as (Starov et al., 2007):

$$\prod_2(h) = \frac{\varepsilon\varepsilon_0(\xi_1-\xi_2)^2}{8\pi h^2} \tag{24}$$

where ε is the relative dielectric permittivity of liquid water (dimensionless), ε_0 is the electric constant in vacuum (F/m), and ξ_1 and ξ_2 are the electric potentials of the solid-liquid and liquid-air interfaces, respectively (V).

The calculation of the structural force can be approximated by a semiempirical equation (Starov et al. 2007; Tuller et al. 1999):

$$\prod_3(h) = ke^{-\frac{\lambda}{h}} \tag{25}$$

where k is the coefficient determining the structural force strength (N/m^2) and λ is the characteristic length of water molecules (nm).

Without loss of generality, in our study, pores are assumed to be cylindrical, homogeneous and isotropic. In cylindrical pores, in addition to the disjoining pressure, the cylindrical capillary forces induced by curved liquid films should be considered. The effective disjoining pressure in a cylindrical capillary is defined as (Mattia et al., 2012):

$$\prod_{eff}(h) = \frac{r}{r-h}\prod_{slit}(h) + \frac{\gamma}{(r-h)} \tag{26}$$

where $\prod_{eff}(h)$ is the effective disjoining pressure within cylindrical pores (MPa), r is the radius of the cylindrical shaped pores (nm), and γ is the surface tension at the interface between gas and liquid water (N/m).

Combining Eqs. (21) and (26), the relationship between h, r and R_h within cylindrical capillaries can be obtained:

$$\frac{r}{r-h}\prod_{slit}(h) + \frac{\gamma}{(r-h)} = -\frac{RT}{V_m^l} ln(R_h) \tag{27}$$

The water saturation of a single cylindrical pore is therefore obtained as follows:

$$w_t(i) = \frac{2h}{r} \tag{28}$$

The values of the parameters used in Eq. (21)- (26) are listed in Table 7 (Churaev, 1995a, 1995b, 2003; Israelachvili, 2011; Takahashi & Kovscek, 2010).

Table 7 Parameters in the calculation of the water film thickness.

Parameter	Symbol	Value	Unit
Temperature	T	313.15	K
Liquid water molar volume	V_m^l	18	cm^3/mol
Hamaker constant (clay-water-air)	A_H	0.8×10^{-20}	J
Relative dielectric constant of water	ε	76.58	-
Electric constant (vacuum)	ε_0	8.85×10^{-12}	F/m
Electric potential difference	$\xi_1 - \xi_2$	50×10^{-3}	V
Coefficient of the structural force	k	1.0×10^{7}	N/m^2
Characteristic decay length of water	λ	1.5	nm
Surface tension	γ	72×10^{-3}	N/m

Li et al. (2016a) determined the distribution of the water saturation in pores of different sizes and suggested that the effect of water on the methane adsorption capacity is mainly attributed to two aspects: (i) small pores (<6 nm) blocked by water are unavailable for methane adsorption and (ii) large pores bounded by water films exhibit a transition from gas-solid to gas-liquid interactions. The

water adsorption measurements in their study referred to the moisture-equilibrated method. It is worth noting that in their research, the relative humidity considered to calculate the water saturation in the different pore sizes was controlled via saturated salt solutions at room temperature (25 ℃) rather than the real relative humidity of gaseous methane. Therefore, the water saturations in the different pore sizes in the PMMS and SAWM experiments should be compared. In the PMMS experiments, as shown in Figure 19, the water saturation in the shale pores varies with the different pore radii and is much higher in pores with smaller radii. Xu et al. (2020) applied a 3-D lattice Boltzmann model to study water adsorption in clay-rich shales, and they concluded that water vapor is preferentially adsorbed in the small and narrow pore spaces. In our study, as shown in Fig. 19, the water saturation in all pores is lower than 1 for R_h< 74.68%, suggesting that the thickness of water film is smaller than the pore radius, and adsorbed water occurs only in the form of water films on pore surfaces. At low water saturations, water resides largely as adsorbed films on pore surfaces and to a lesser extent as pendular rings at grain-rain contact points (Tokunaga et al., 2017a). It can also be observed that the water saturation in pores with radii ranging from 0.37–3.81 nm equals 1 at an R_h level of 96.41%, indicating that the thickness of water film is larger than the pore radius. Hence, these pores are completely filled with water.

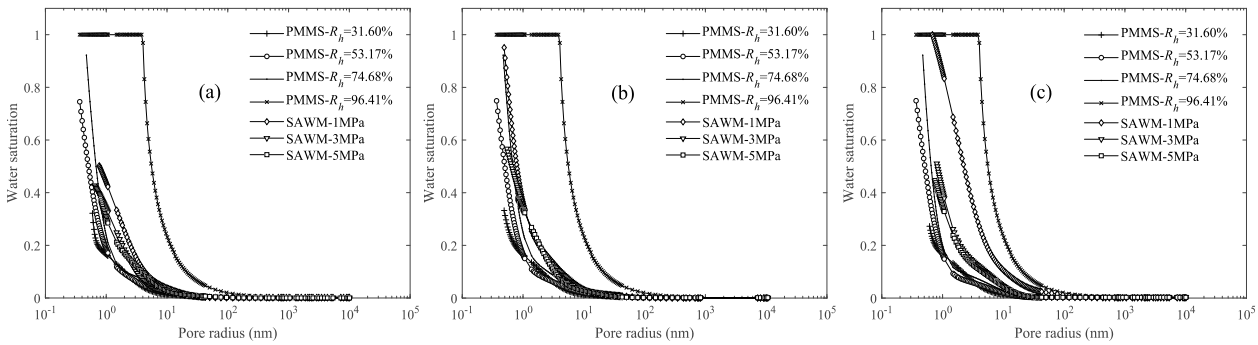

Figure 19. Water saturation under the different pore radii. (a) S1, (b) S2, (c) S3.

The equilibrium relative humidity in the SAWM experiments is presented in Table 8, which decreases with increasing pressure. Figure 20 shows that under the same pressure, the equilibrium relative humidity (ER_h) is negatively correlated with the I/S content and is positively correlated with R_o. Organic matter such as kerogen usually possesses more hydrophobic sites, and the maturity of kerogen is indicated by R_o (Wang & Yu, 2016). Hydrophobic sites are well developed in highly mature samples. Therefore, the number of hydrophobic sorption sites throughout the pore network of the samples is positively correlated with ER_h. The hydrophobicity of S3 is the highest, leading

to a smaller reduction in the equilibrium R_h value. Figure 19 shows that for S1 and S2 in the SAWM experiments, the water saturation in all pores is lower than 1 at 1, 3 and 5 MPa, suggesting that the thickness of water film is smaller than the pore radius, and adsorbed water only occurs in the form of water films on pore surfaces. For S3 in the SAWM experiments, some fine pores are fully filled with water under 1MPa, although the pore size range fully filled with water is relative narrow. A reasonable explanation for this phenomenon is that water vapor diffusion and adsorption ensue inadequately in micropores due to the hydrophobicity of S3, and water tends to occur as droplets (Cailliez et al., 2008; Wang et al., 2020). When water droplets completely block narrow pore throat regions, methane can hardly penetrate the water barrier, which is unfavorable for methane diffusion and adsorption. As a result, in addition to R_h and the pore size distribution, the hydrophobicity of shale is also a key factor influencing the water distribution.

Table 8 Equilibrium relative humidity in the SAWM experiments.

Pressure (MPa)	S1	S2	S3
1	0.824	0.825	0.936
3	0.705	0.791	0.842
5	0.740	0.757	0.812

As shown Figure 19, the accessibility of pore radii smaller than 1 nm to water vapor in the SAWM experiments is inferior to that in the PMMS experiments, namely, water vapor can occupy and fill micropores more easily in the premoistening procedure. Ruppert et al. (2013) separately identified the accessibility of clay-rich shale pores to deuterated methane and deuterated water via ultrasmall-angle neutron scattering and suggested that pores smaller than 30 nm exhibit a higher affinity for water than for methane. Yang et al. (2020) proposed a multiscale approach combining molecular simulation and the lattice Boltzmann method to study gas migration in shale nanopores. Their results indicated that the maximum adsorbed gas density occurs in pores with a size of 4 nm. In addition to Langmuir single-layer adsorption, the adsorption mechanism involving pore filling also occurs in micropores (< 2 nm). The micropore volume and SSA provide more sites for methane adsorption (Heller & Zoback, 2014; Liu et al., 2016). The large SSA and micropores of inorganic or organic matter are the main overlap areas between water and methane adsorption (Jin & Firoozabadi, 2014; Wang et al., 2020). The above observations suggest that in the PMMS experiments, preadsorbed water obviously lowers the methane adsorption amount and rate through the occupation of micropores (0.3–1.5 nm), which renders microporous adsorption sites unavailable

to methane. Thus, methane fails to form the same multilayer on surfaces occupied by preadsorbed water, and is mainly adsorbed in pores with radii larger than 1.5 nm. Figure 19 also shows that in the SAWM experiments, water largely occupies the mesopores (1.5–20 nm). This occurs because methane with a high partial pressure carries water vapor to the shale surface, methane molecules preferentially occupy the micropores, and competitive adsorption between methane and water vapor mainly occurs on the surface of mesopores (1.5–20 nm). In addition, the influence of water on pores with radii larger than 100 nm is slight, which results from the low water film coverage.

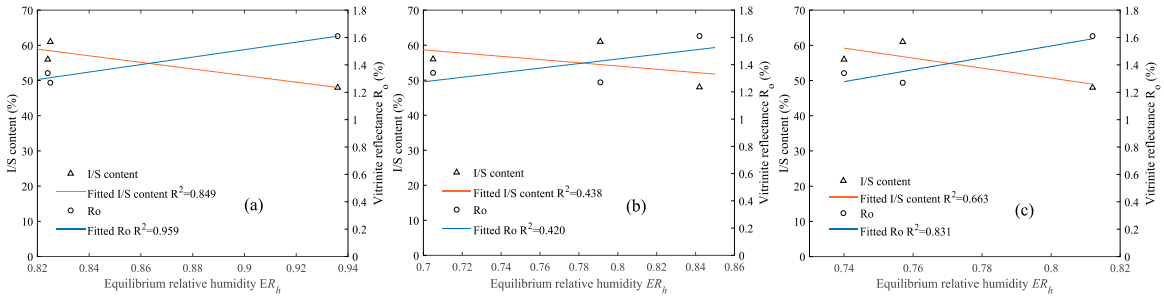

Figure 20. Relationship between the equilibrium relative humidity ER_h and the I/S content and R_o. (a) 1MPa, (b) 3MPa, (c) 5MPa.

4 Conclusions

Experiments involving pure methane adsorption onto dry shale (PMD), pure methane adsorption onto moisture-equilibrated shale (PMMS) and simultaneous adsorption of water vapor and methane (SAWM) onto shale were conducted to investigate: (1) the differences in the effects of water vapor and preadsorbed water on methane adsorption; (2) the distributions of adsorbed methane and water in shale pores; (3) the mechanisms of water-methane-shale interaction in the PMMS and SAWM processes. Several findings were obtained based on the experimental and calculation results.

1. The impact of water vapor and preadsorbed water on the methane adsorption capacity of the shale samples was quantified. Compared to the methane adsorption capacity in the PMD experiments, the equilibrium methane adsorption reduction amount ranges from 81–96% in the PMMS experiments and from 20–49% in the SAWM experiments. Preadsorbed water reduces the methane adsorption capacity more notably than does water vapor. The micro- and mesopore volumes are positively correlated with the equilibrium methane adsorption reduction amount in the PMMS experiments, while the micro- and mesopore volumes are negatively and inconspicuously correlated with the equilibrium methane adsorption reduction amount in the SAWM experiments. Correlation analysis suggests that the influences of preadsorbed water and water vapor on the

methane adsorption capacity are different in regard to pore channel blocking: the blocking effect induced by water vapor on micro- to mesopores is weaker than that induced by preadsorbed water.

2. The equilibrium methane adsorption amount in the SAWM experiments is notably larger than that in the PMMS experiments at the same water content. In the PMMS experiments, the methane adsorption amount decreases with increasing water content, the impact of preadsorbed water on methane adsorption amount becomes less obvious when the water content exceeds the critical value, and the critical values for S1, S2 and S3 are 1.49, 1.07 and 0.88 mmol/g, respectively. In the SAWM experiments, the equilibrium adsorption amount of water vapor is 2.5–24 times that of methane. With increasing water content, the equilibrium methane adsorption amount does not decrease as notably as that in the PMMS experiments. This indicates that water vapor adsorption is inhibited by methane, and the critical water content of the samples is not reached in the SAWM experiments.

3. The results of water film thickness calculation suggest that the accessibility of pores with radii smaller than 1 nm to water vapor in the SAWM experiments is inferior to that in the PMMS. In the PMMS experiments, preadsorbed water lowers the methane adsorption capacity through the occupation of micropores (0.3–1.5 nm), and methane is largely adsorbed in pores with radii larger than 1.5 nm due to the unavailability of micropores. The increase in water film thickness in the premoistening procedure triggers the water blocking effect, narrows or even blocks methane diffusion pathways, and seriously reduces the methane concentration gradient and methane-shale surface interaction. In the SAWM experiments, methane preferentially occupies the micropores, and water vapor mainly occupies the mesopores (1.5–20 nm) due to competition with methane. In the SAWM experiments, water vapor diffusion and adsorption in the pores are inhibited by the high methane partial pressure, and water molecules do not block pore channels nor occupy adsorption sites in advance, as was observed in the PMMS experiments.

4. To distinguish the impact of water vapor and preadsorbed water on the methane adsorption rate, the time required for methane to reach 10%, 50%, 80% and 95% of the equilibrium adsorption amount in the PMD, PMMS and SAWM experiments was compared. The results suggest that methane reaches adsorption equilibrium the fastest in the PMD experiments. In the PMMS experiments, the time required for methane to reach adsorption equilibrium increases with increasing water content. The methane adsorption rate in the SAWM experiments is higher than that in the PMMS experiments before the equilibration degree reaches 95%. In contrast, when the

equilibration degree exceeds 95%, water vapor can replace some of the adsorbed methane molecules via the volume displacement effect. The comparison of the methane adsorption rates between the PMMS and SAWM experiments suggests that the detrimental effect of preadsorbed water on the methane adsorption rate is more obvious than that of water vapor. In the PMMS experiments, the influence of preadsorbed water on the methane adsorption rate is largely reflected by the observed resistance and blocking effects. In the SAWM experiments, the influence of water vapor on the methane adsorption rate is mainly reflected by the inhibition and competition effects.

5. In the PMMS experiments, the methane adsorption rate distinctly decreases as a linear function of the equilibration degree followed by fluctuation. In the SAWM experiments, the methane adsorption rate rapidly decreases in a linear manner with the equilibration degree followed by fluctuation, and the water vapor adsorption rate decreases exponentially with the equilibration degree. The deviation in variation in the methane and water vapor adsorption rates in the SAWM experiments results from the partial pressure difference and the distinct methane-shale and water-shale interaction mechanisms.

Acknowledgments

The authors are very grateful for the help from the Rock Fracture Workgroup. This study was funded by the National Natural Sciences Foundation of China (Grant Nos. 41877196, U1612441 and 41272387) and the Fundamental Research Funds for the Central Universities of China (Grant No. 53200759753).

Data Availability Statement

The data for figures in this research are available online: https://doi.org/10.5281/zenodo.5196112.

References

Berghe, G., Kline, S., Burket, S., Bivens, L., Johnson, D., & Singh, R. (2019). Effect of CO_2 and H_2O on the behavior of shale gas confined inside calcite [104] slit-like nanopore: a molecular dynamics simulation study. *Journal of Molecular Modeling*, *25*(9), 293. https://doi.org/10.1007/s00894-019-4180-7.

Cailliez, F., Stirnemann, G., Boutin, A., Demachy, I., & Fuchs, A. H. (2008). Does Water Condense in Hydrophobic Cavities? A Molecular Simulation Study of Hydration in Heterogeneous Nanopores. *The Journal of Physical Chemistry C*, *112*(28), 10435-10445. https://doi.org/10.1021/jp710746b.

Chalmers, G. R. L., & Bustin, R. M. (2007). The organic matter distribution and methane capacity of

the Lower Cretaceous strata of Northeastern British Columbia, Canada. *International Journal of Coal Geology*, *70*(1-3), 223-239. https://doi.org/10.1016/j.coal.2006.05.001.

Churaev, N. V. (1995a). Contact angles and surface forces. *Advances in Colloid and Interface Science*, *58*(2), 87-118. https://doi.org/10.1016/0001-8686(95)00245-L.

Churaev, N. V. (1995b). The Relation between Colloid Stability and Wetting. *Journal of Colloid and Interface Science*, *172*(2), 479-484. https://doi.org/10.1006/jcis.1995.1278.

Churaev, N. V. (2003). Surface Forces in Wetting Films. *Colloid Journal*, *65*(3), 263-274. https://doi.org/10.1023/A:1024292618059.

Churaev, N. V., Starke, G., & Adolphs, J. (2000). Isotherms of Capillary Condensation Influenced by Formation of Adsorption Films: 1. Calculation for Model Cylindrical and Slit Pores. *Journal of Colloid and Interface Science*, *221*(2), 246-253. https://doi.org/10.1006/jcis.1999.6592.

Curtis, M., Ambrose, R., Sondergeld, C., & Rai, C. (2011). *Transmission and Scanning Electron Microscopy Investigation of Pore Connectivity of Gas Shales on the Nanoscale*. Paper presented at North American Unconventional Gas Conference and Exhibition, Texas, USA. https://doi.org/10.2118/144391-MS.

Daridon, J. L., Lagourette, B., Saint-Guirons, H., & Xans, P. (1993). A cubic equation of state model for phase equilibrium calculation of alkane + carbon dioxide + water using a group contribution k_{ij}. *Fluid Phase Equilibria*, *91*(1), 31-54. https://doi.org/10.1016/0378-3812(93)85077-Y.

Dasani, D., Wang, Y., Tsotsis, T. T., & Jessen, K. (2017). Laboratory-Scale Investigation of Sorption Kinetics of Methane/Ethane Mixtures in Shale. *Industrial & Engineering Chemistry Research*, *56*(36), 9953-9963. https://doi.org/10.1021/acs.iecr.7b02431.

Derjaguin, B. V., Churaev, N. V., & Muller, V. M. (1987). The Theory of Heterocoagulation in Lyophobic Systems. In B. V. Derjaguin, N. V. Churaev, & V. M. Muller (Eds.), *Surface Forces* (pp. 311-326). Boston, MA: Springer US. https://doi.org/10.1007/978-1-4757-6639-4_9.

Dhima, A., de Hemptinne, J. C., & Moracchini, G. (1998). Solubility of light hydrocarbons and their mixtures in pure water under high pressure. *Fluid Phase Equilibria*, *145*(1), 129-150. https://doi.org/10.1016/S0378-3812(97)00211-2.

Dhima, A., de Hemptinne, J. C., & Jose, J. (1999). Solubility of hydrocarbons and CO_2 mixtures in water under high pressure. *Industrial & Engineering Chemistry Research*, *38*(8), 3144-3161. https://doi.org/10.1021/ie980768g.

Do, D. D., & Do, H. D. (2003). Pore characterization of carbonaceous materials by DFT and GCMC simulations: A review. *Adsorption Science & Technology*, *21*(5), 389-423. https://doi.org/10.1260/026361703769645753.

Feng, D., Li, X., Wang, X., Li, J., Sun, F., Sun, Z., et al. (2018). Water adsorption and its impact on the pore structure characteristics of shale clay. *Applied Clay Science*, *155*, 126-138. https://doi.org/10.1016/j.clay.2018.01.017.

Gao, J., & Yu, Q. (2018). Effect of Water Saturation on Pressure-Dependent Permeability of Carboniferous Shale of the Qaidam Basin, China. *Transport in Porous Media*, *123*(1), 147-172. https://doi.org/10.1007/s11242-018-1029-y.

Gasparik, M., Ghanizadeh, A., Bertier, P., Gensterblum, Y., Bouw, S., & Krooss, B. M. (2012). High-Pressure Methane Sorption Isotherms of Black Shales from The Netherlands. *Energy & Fuels*, *26*(8), 4995-5004. https://doi.org/10.1021/ef300405g.

Gasparik, M., Bertier, P., Gensterblum, Y., Ghanizadeh, A., Krooss, B. M., & Littke, R. (2014). Geological controls on the methane storage capacity in organic-rich shales. *International Journal of Coal Geology*, *123*, 34-51. https://doi.org/10.1016/j.coal.2013.06.010.

Gensterblum, Y., Busch, A., & Krooss, B. M. (2014). Molecular concept and experimental evidence of competitive adsorption of H_2O, CO_2 and CH_4 on organic material. *Fuel*, *115*, 581-588. https://doi.org/10.1016/j.fuel.2013.07.014.

Greenspan, L. (1977). Humidity Fixed Points of Binary Saturated Aqueous Solutions. *Journal of Research of the National Bureau of Standards Section A: Physics and Chemistry*, *81A(1)*, 89-96. https://doi.org/10.6028/jres.081A.011.

Heller, R., & Zoback, M. Zoback (2014). Adsorption of methane and carbon dioxide on gas shale and pure mineral samples. *Journal of Unconventional Oil and Gas Resources*, *8*, 14-24. https://doi.org/10.1016/j.juogr.2014.06.001.

Israelachvili, J. N. (2011). Chapter 14 - Electrostatic Forces between Surfaces in Liquids. In J. N. Israelachvili (Eds.), *Intermolecular and Surface Forces (Third Edition)* (pp. 291-340). San Diego: Academic Press. https://doi.org/10.1016/B978-0-12-375182-9.10014-4.

Ji, L., Zhang, T., Milliken, K. L., Qu, J., & Zhang, X. (2012). Experimental investigation of main controls to methane adsorption in clay-rich rocks. *Applied Geochemistry*, *27*(12), 2533-2545. https://doi.org/10.1016/j.apgeochem.2012.08.027.

Jin, Z., & Firoozabadi, A. (2014). Effect of water on methane and carbon dioxide sorption in clay minerals by Monte Carlo simulations. *Fluid Phase Equilibria*, *382*, 10-20. https://doi.org/10.1016/j.fluid.2014.07.035.

Kuchler, M. (2017). Post-conventional energy futures: Rendering Europe's shale gas resources governable. *Energy Research & Social Science*, *31,* 32-40. https://doi.org/10.1016/j.erss.2017.05.028.

Li, J., Li, X., Wang, X., Li, Y., Wu, K., Shi, J., et al. (2016a). Water Distribution Characteristic and Effect on Methane Adsorption Capacity in Shale Clays. *International Journal of Coal Geology*, *159*, 135-154. https://doi.org/10.1016/j.coal.2016.03.012.

Li, J., Li, X., Wu, K., Wang, X., Shi, J., Yang, L., et al. (2016b). Water Sorption and Distribution Characteristics in Clay and Shale: Effect of Surface Force. *Energy & Fuels*, *30*(11), 8863-8874. https://doi.org/10.1021/acs.energyfuels.6b00927.

Liu, J., Xi, S., & Chapman, W. G. (2019). Competitive Sorption of CO_2 with Gas Mixtures in Nanoporous Shale for Enhanced Gas Recovery from Density Functional Theory. *Langmuir*, *35*(24), 8144-8158. https://doi.org/10.1021/acs.langmuir.9b00410.

Liu, Y., Zhu, Y., Li, W., Xiang, J., Wang, Y., Li, J., & Zeng, F. (2016). Molecular simulation of methane adsorption in shale based on grand canonical Monte Carlo method and pore size distribution. *Journal of Natural Gas Science and Engineering*, *30*, 119-126. https://doi.org/10.1016/j.jngse.2016.01.046.

Ma, L., & Yu, Q. (2020). Dynamic behaviors of methane adsorption on partially saturated shales. *Journal of Petroleum Science and Engineering*, *190*, 107071. https://doi.org/10.1016/j.petrol.2020.107071.

Mattia, D., Starov, V., & Semenov, S. (2012). Thickness, stability and contact angle of liquid films on and inside nanofibres, nanotubes and nanochannels. *Journal of Colloid and Interface Science*, *384*(1), 149-156. https://doi.org/10.1016/j.jcis.2012.06.051.

Merkel, A., Fink, R., & Littke, R. (2015). The role of pre-adsorbed water on methane sorption capacity of Bossier and Haynesville shales. *International Journal of Coal Geology*, *147-148*, 1-8. https://doi.org/10.1016/j.coal.2015.06.003.

Merkel, A., Fink, R., & Littke, R. (2016). High pressure methane sorption characteristics of lacustrine shales from the Midland Valley Basin, Scotland. *Fuel*, *182*, 361-372.

https://doi.org/10.1016/j.fuel.2016.05.118.

Peng, D. -Y., & Robinson, D. B. (1976). A New Two-Constant Equation of State. *Industrial & Engineering Chemistry Fundamentals*, *15*(1), 59-64. https://doi.org/10.1021/i160057a011.

Rani, S., Prusty, B. K., & Pal, S. K. (2018). Adsorption kinetics and diffusion modeling of CH_4 and CO_2 in Indian shales. *Fuel*, *216*, 61-70. https://doi.org/10.1016/j.fuel.2017.11.124.

Ross, D. J. K., & Marc Bustin, R. (2009). The importance of shale composition and pore structure upon gas storage potential of shale gas reservoirs. *Marine and Petroleum Geology*, *26*(6), 916-927. https://doi.org/10.1016/j.marpetgeo.2008.06.004.

Ruppert, L. F., Sakurovs, R., Blach, T. P., He, L., Melnichenko, Y. B., Mildner, D. F. R., & Alcantar-Lopez, L. (2013). A USANS/SANS Study of the Accessibility of Pores in the Barnett Shale to Methane and Water. *Energy & Fuels*, *27*(2), 772-779. https://doi.org/10.1021/ef301859s.

Sang, G., Liu, S., & Elsworth, D. (2019). Water Vapor Sorption Properties of Illinois Shales Under Dynamic Water Vapor Conditions: Experimentation and Modeling. *Water Resources Research*, *55*(8), 7212-7228. https://doi.org/10.1029/2019WR024992.

Sangwichien, C., Aranovich, G. L., & Donohue, M. D. (2002). Density functional theory predictions of adsorption isotherms with hysteresis loops. *Colloids and Surfaces A: Physicochemical and Engineering Aspects*, *206*(1), 313-320. https://doi.org/10.1016/S0927-7757(02)00048-1.

Schlömer, S., & Krooss, B. M. (1997). Experimental characterisation of the hydrocarbon sealing efficiency of cap rocks. *Marine and Petroleum Geology*, *14*(5), 565-580. https://doi.org/10.1016/S0264-8172(97)00022-6.

Shibue, Y. (2003). Vapor pressures of aqueous NaCl and $CaCl_2$ solutions at elevated temperatures. *Fluid Phase Equilibria*, *213*(1-2), 39-51. https://doi.org/10.1016/S0378-3812(03)00284-X.

Sing, K. S. W., Everett, D. H., Haul, R. A. W., Moscou, L., Pierotti, R. A., Rouquerol, J., & Siemieniewska, T. (1985). Reporting Physisorption Data for Gas Solid Systems with Special Reference to the Determination of Surface-Area and Porosity (Recommendations 1984). *Pure and Applied Chemistry*, *57*(4), 603-619. https://doi.org/10.1351/pac198557040603.

Singh, H. (2016). A critical review of water uptake by shales. *Journal of Natural Gas Science and Engineering*, *34*, 751-766. https://doi.org/10.1016/j.jngse.2016.07.003.

Søreide, I., & Whitson, C. (1992). Peng-Robinson predictions for hydrocarbons, CO_2, N_2, and H_2S with pure water and NaCl brine. *Fluid Phase Equilibria*, *77*, 217-240. https://doi.org/10.1016/0378-

3812(92)85105-H.

Starov, V. M., Velarde, M. G., & Radke, C. J. (2007). *Wetting and Spreading Dynamics* (1st ed.). Boca Raton: CRC Press. https://doi.org/10.1201/9781420016178.

Stryjek, R., & Vera, J. H. (1986). Prsv - an Improved Peng-Robinson Equation of State for Pure Compounds and Mixtures. *Canadian Journal of Chemical Engineering*, *64*(2), 323-333. https://doi.org/10.1002/cjce.5450640224.

Sun, Z., Zhou, S., Li, J., Chen, K., Zhang, C., Zhang, Y., & Li, P. (2020). Laboratory Research on Gas Transport in Shale Nanopores Considering the Stress Effect and Slippage Effect. *Journal of Geophysical Research: Solid Earth*, *125*(5), e2019JB018256. https://doi.org/10.1029/2019JB018256.

Švábová, M., Weishauptová, Z., & Přibyl, O. (2011). Water vapour adsorption on coal. *Fuel*, *90*, 1892-1899. https://doi.org/10.1016/j.fuel.2011.01.005.

Takahashi, S., & Kovscek, A. R. (2010). Wettability estimation of low-permeability, siliceous shale using surface forces. *Journal of Petroleum Science and Engineering*, *75*(1), 33-43. https://doi.org/10.1016/j.petrol.2010.10.008.

Tokunaga, T. K., Finsterle, S., Kim, Y., Wan, J., Lanzirotti, A., & Newville, M. (2017a). Ion Diffusion Within Water Films in Unsaturated Porous Media. *Environmental Science & Technology*, *51*(8), 4338-4346. https://doi.org/10.1021/acs.est.6b05891.

Tokunaga, T. K., Shen, W., Wan, J., Kim, Y., Cihan, A., Zhang, Y., & Finsterle, S. (2017b). Water Saturation Relations and Their Diffusion-Limited Equilibration in Gas Shale: Implications for Gas Flow in Unconventional Reservoirs. *Water Resources Research*, *53*(11), 9757-9770. https://doi.org/10.1002/2017WR021153.

Tsang, C. F., Barnichon, J. D., Birkholzer, J., Li, X. L., Liu, H. H., & Sillen, X. (2012). Coupled thermo-hydro-mechanical processes in the near field of a high-level radioactive waste repository in clay formations. *International Journal of Rock Mechanics and Mining Sciences*, *49*, 31-44. https://doi.org/10.1016/j.ijrmms.2011.09.015.

Tuller, M., Dani, O., & Dudley, L. M. (1999). Adsorption and capillary condensation in porous media: Liquid retention and interfacial configurations in angular pores. *Water Resources Research*, *35*(7), 1949-1964. https://doi.org/10.1029/1999WR900098.

Vengosh, A., Jackson, R. B., Warner, N., Darrah, T. H., & Kondash, A. (2014). A Critical Review of the

Risks to Water Resources from Unconventional Shale Gas Development and Hydraulic Fracturing in the United States. *Environmental Science & Technology*, *48*(15), 8334-8348. https://doi.org/10.1021/es405118y.

Wang, F., Yao, Y., Wen, Z., Sun, Q., & Yuan, X. (2020). Effect of water occurrences on methane adsorption capacity of coal: A comparison between bituminous coal and anthracite coal. *Fuel*, *266*, 117102. https://doi.org/10.1016/j.fuel.2020.117102.

Wang, L., & Yu, Q. (2016). The effect of moisture on the methane adsorption capacity of shales: A study case in the eastern Qaidam Basin in China. *Journal of Hydrology*, *542*, 487-505. https://doi.org/10.1016/j.jhydrol.2016.09.018.

Wang, L., Wan, J., Tokunaga, T. K., Kim, Y., & Yu, Q. (2018). Experimental and Modeling Study of Methane Adsorption onto Partially Saturated Shales. *Water Resources Research*, *54*(7), 5017-5029. https://doi.org/10.1029/2017WR020826.

Wang, M., & Yu, Q. (2019). A method to determine the permeability of shales by using the dynamic process data of methane adsorption. *Engineering Geology*, *253*, 111-122. https://doi.org/10.1016/j.enggeo.2019.03.015.

Wang, M., & Yu, Q. (2020). Comparing the permeability of dry and moisturized crushed shales determined by the dynamic process data of methane adsorption. *Journal of Hydrology*, *590*, 125375. https://doi.org/10.1016/j.jhydrol.2020.125375.

Wang, X. K., Zhou, Y., Li, L., Gao, T. C., & Tang, N. (2015). Modelling the Natural Evaporation of the Concentrated Seawater after Desalinized. *Applied Mechanics and Materials*, *713-715*, 2989-2992. https://doi.org/10.4028/www.scientific.net/AMM.713-715.2989.

Xu, R., Prodanović, M., & Landry, C. (2020). Pore-Scale Study of Water Adsorption and Subsequent Methane Transport in Clay in the Presence of Wettability Heterogeneity. *Water Resources Research*, *56*(10), e2020WR027568. https://doi.org/10.1029/2020WR027568.

Yang, F., Xie, C., Ning, Z., & Krooss, B. M. (2017). High-Pressure Methane Sorption on Dry and Moisture-Equilibrated Shales. *Energy & Fuels*, *31*(1), 482-492. https://doi.org/10.1021/acs.energyfuels.6b02999.

Yang, S., & Yu, Q. (2020). Experimental Investigation on the Movability of Water in Shale Nanopores: A Case Study of Carboniferous Shale From the Qaidam Basin, China. *Water Resources Research*, *56*(8), e2019WR026973. https://doi.org/10.1029/2019WR026973.

Yang, X., Zhou, W., Liu, X., & Yan, Y. (2020). A multiscale approach for simulation of shale gas transport in organic nanopores. *Energy*, *210*, 118547. https://doi.org/10.1016/j.energy.2020.118547. https://doi.org/10.1016/j.energy.2020.118547.

Yuan, W., Li, X., Pan, Z., Connell, L. D., Li, S., & He, J. (2014a). Experimental Investigation of Interactions between Water and a Lower Silurian Chinese Shale, *Energ Fuel*, *28*(8), 4925-4933. https://doi.org/10.1021/ef500915k.

Yuan, W., Pan, Z., Li, X., Yang, Y., Zhao, C., Connell, L. D., et al. (2014b). Experimental study and modelling of methane adsorption and diffusion in shale. *Fuel*, *117*, 509-519. https://doi.org/10.1016/j.fuel.2013.09.046.

ZareNezhad, B., & Eggeman, T. (2006). Application of Peng-Rabinson equation of state for CO_2 freezing prediction of hydrocarbon mixtures at cryogenic conditions of gas plants. *Cryogenics*, *46*(12), 840-845. https://doi.org/10.1016/j.cryogenics.2006.07.010.

Zhang, T., Javadpour, F., Yin, Y., & Li, X. (2020). Upscaling Water Flow in Composite Nanoporous Shale Matrix Using Lattice Boltzmann Method. *Water Resources Research*, *56*(4), e2019WR026007. https://doi.org/10.1029/2019WR026007.

Zhou, L., Zhou, Y., Li, M., Chen, P., & Wang, Y. (2000). Experimental and Modeling Study of the Adsorption of Supercritical Methane on a High Surface Activated Carbon. *Langmuir*, *16*(14), 5955-5959. https://doi.org/10.1021/la991159w.

Zou, J., Rezaee, R., & Yuan, Y. (2018). Investigation on the adsorption kinetics and diffusion of methane in shale samples. *Journal of Petroleum Science and Engineering*, *171*, 951-958. https://doi.org/10.1016/j.petrol.2018.08.010.